Inertial Oscillations Disintegrating Coherent Vortices

JIM THOMAS,[a,b] AMJAD HASAN,[a] AND RAJENDRA S. RAJPOOT[b]

[a] *International Centre for Theoretical Sciences, Tata Institute of Fundamental Research, Bangalore, India*
[b] *Centre for Applicable Mathematics, Tata Institute of Fundamental Research, Bangalore, India*

(Manuscript received 16 January 2025, in final form 15 April 2026, accepted 27 April 2026)

ABSTRACT: We study the disintegration of coherent vortices due to interaction with inertial oscillations using a two-vertical-mode model. For this, we generated and examined 640 flow regimes by varying the Rossby number and baroclinic–barotropic energy ratio. Based on the study, we find that increasing the Rossby number while keeping the same energy ratio and increasing the energy ratio at the same Rossby number can lead to faster disintegration of vortices. Exploring physical space regions partitioned into strain-dominant and vorticity-dominant regions, we see that disintegrating vortices have forward energy flux located in strain-dominant regions, while slightly weaker inverse energy flux is seen in vorticity-dominant regions. The net effect results in a forward cascade of the flow. Multiple phenomenological changes in the disintegration process are also seen on comparing anticyclonic and cyclonic vortices. The findings of this study in general help develop an understanding of the energy levels and Rossby number needed for unbalanced flows to disintegrate balanced flows in a broad regime going from small to $O(1)$ Rossby numbers, this being the Rossby number transition seen as we move from mesoscales to submesoscales in the world's oceans.

KEYWORDS: Eddies; Internal waves; Mesoscale processes; Turbulence

1. Introduction

Fast-evolving dispersive internal gravity waves and slowly evolving balanced eddies are major flow components at oceanic mesoscales and submesoscales. Instabilities of the basin-scale flow generate balanced eddies, and once formed, these eddies are constrained by geostrophic and hydrostatic balance. These balances prevent a forward energy cascade for the balanced flow, leading to eddy dissipation requiring the intervention of lateral or bottom boundaries (Arbic et al. 2009; Zhai et al. 2010; Nikurashin et al. 2013). Internal waves, on the other hand, are characterized by a forward energy cascade and dissipation at small scales, leading to ocean mixing (Gregg et al. 2003; Whalen et al. 2020; MacKinnon et al. 2017).

In regions that are far from boundaries, internal gravity waves could interact with balanced eddies and facilitate their breakdown and dissipation. This hypothesis has gained impetus over the past two decades with in situ measurements, satellite datasets, and realistic ocean models revealing the presence of energetic internal wave fields in different oceanic regions. Notably, several observations reveal that wave energy levels could be as high and sometimes higher than balanced energy levels, depending on geographic location and season (Pinkel 2014; Qiu et al. 2017; Savage et al. 2017; Tchilibou et al. 2018; Torres et al. 2018; Cao et al. 2019; Yu et al. 2019; Lien and Sanford 2019; Qiu et al. 2022; Vladoiu et al. 2024). Inspired by these observations, a broad set of studies have examined how different kinds of waves affect balanced flow dynamics. Asymptotic and numerical studies reveal that in the low Rossby number regime, disrupting and dissipating balanced flow requires unbalanced energy levels to be much higher than balanced flow (see theoretical and numerical results detailed in Thomas 2023). Balanced flows in the low Rossby number regime are more rugged in this sense. Despite the matured level of understanding achieved for the low Rossby number regime, as applicable to the mesoscale flows, relatively less is understood regarding the unbalanced energy level needed to disrupt balanced flows as the Rossby number increases. Exploring this in a specific setup is the goal of the present work.

As mentioned above, internal waves with different frequencies are generated in the ocean. Among these, inertial oscillations are the lowest-frequency modes that are excited by atmospheric winds and storms in the upper ocean. Close to one terawatt of power goes into the near-inertial band in the internal wave frequency spectra (Alford 2001; Watanabe and Hibiya 2002), making these unbalanced motions a prominent feature in the world's oceans. Pure inertial oscillations are associated with closed-circle particle trajectories and can stay in a specific region for long times. However, interaction with eddies and other currents can transform inertial oscillations into large-horizontal-scale near-inertial waves that can radiate away. Given their dominant presence in the oceans, multiple past studies have examined interactions between inertial oscillations and balanced flows with the hope of uncovering mechanisms by which these unbalanced flows can facilitate the breakdown of balanced flows (Gertz and Straub 2009; Taylor and Straub 2020; Thomas and Arun 2020; Thomas and Daniel 2020; Wagner and Young 2016; Rocha et al. 2018; Thomas and Vishnu 2022; Barkan et al. 2017).

Among the abovementioned studies, Thomas and Vishnu (2022) used a two-vertical-mode model, obtained by projecting the hydrostatic Boussinesq equations on the barotropic and a high baroclinic mode, to study energetic interactions between inertial oscillations and balanced flow. They kept the unbalanced-to-balanced energy ratio asymptotically small and varied the Rossby number to find that, at high Rossby numbers, a small amount of unbalanced baroclinic energy was sufficient

Corresponding author: Jim Thomas, jimthomas.edu@gmail.com

DOI: 10.1175/JPO-D-24-0256.1

to disrupt and dissipate energetic barotropic flows. This finding has also been noticed in more complex ocean models. For instance, Capet et al. (2008) point out that low unbalanced energy could trigger a forward energy flux of a submesoscale flow.

In this study, we explore how inertial oscillations interact with coherent barotropic vortices across different wave-balance energy ratios and Rossby numbers. While previous studies either fixed the Rossby number and varied the wave-balanced energy ratio (Thomas and Daniel 2020, for example) or fixed the wave-balanced energy ratio and varied the Rossby number (Thomas and Vishnu 2022, for example), the present work explores a broad parameter regime in which we vary both the wave-balanced energy ratio and the Rossby number. In particular, our focus is on figuring out the minimum unbalanced energy required to disintegrate an eddy at a given Rossby number.

As part of this study, we use a Gaussian barotropic vortex with unit energy as a coherent eddy, while the inertial oscillations are confined to a single high baroclinic mode in the two-vertical-mode model used by Thomas and Vishnu (2022). The equations are then numerically integrated with different energy levels for inertial oscillations while the Rossby number is increased from 0.1 to 1. We perform similar experiments for anticyclonic and cyclonic vortices to examine the differences in the vortex breakdown features.

The plan for the manuscript is as follows: We discuss the equations in section 2, numerical details and flow initializations in section 3, vortex disintegration details in section 4, physical structure of the flow in section 5, inertial oscillation dynamics in section 6, energy transfers and flux in section 7, and summarize our findings in section 8.

2. Equations and nondimensionalization

The f-plane hydrostatic Boussinesq equations are

$$\frac{\partial \mathbf{v}}{\partial t} + \mathbf{f}\times\mathbf{v} + \nabla p + \mathbf{v}\cdot\nabla\mathbf{v} + w\frac{\partial \mathbf{v}}{\partial z} = 0, \tag{1a}$$

$$\frac{\partial b}{\partial t} + N^2 w + \mathbf{v}\cdot\nabla b + w\frac{\partial b}{\partial z} = 0, \tag{1b}$$

$$\frac{\partial p}{\partial z} = b, \tag{1c}$$

$$\nabla\cdot\mathbf{v} + \frac{\partial w}{\partial z} = 0, \tag{1d}$$

where $\mathbf{v}$ and w are the horizontal and vertical velocities, p is the pressure, and b is the buoyancy; $\mathbf{f} = f\hat{\mathbf{z}}$ with f being the constant Coriolis frequency and $\hat{\mathbf{z}}$ is the unit vector along the z direction. The constant buoyancy frequency is N, and $\nabla = (\partial/\partial x, \partial/\partial y)$ is the gradient operator.

To construct a two-vertical-mode model, we constrain the flow to two vertical modes: barotropic and an nth baroclinic mode (see the procedure detailed in Frierson et al. 2004, for example). For this, we expand variables as

$$(\mathbf{v}, p) = (\mathbf{v}_T, p_T) + \sqrt{2}(\mathbf{v}_C, p_C)\cos\left(\frac{n\pi z}{H}\right), \tag{2a}$$

$$(w, b) = \sqrt{2}(w_C, b_C)\sin\left(\frac{n\pi z}{H}\right). \tag{2b}$$

The subscripts "T" and "C" above denote barotropic and baroclinic variables, respectively. Substituting the above expansion in (1) and writing down terms that project on the barotropic and the first baroclinic mode, after ignoring all other vertical modes, leads to

$$\frac{\partial \mathbf{v}_T}{\partial t} + \mathbf{f}\times\mathbf{v}_T + \nabla p_T + \mathbf{v}_T\cdot\nabla\mathbf{v}_T + \mathbf{v}_C\cdot\nabla\mathbf{v}_C + (\nabla\cdot\mathbf{v}_C)\mathbf{v}_C = 0, \tag{3a}$$

$$\nabla\cdot\mathbf{v}_T = 0, \tag{3b}$$

$$\frac{\partial \mathbf{v}_C}{\partial t} + \mathbf{f}\times\mathbf{v}_C + \nabla p_C + (\mathbf{v}_T\cdot\nabla\mathbf{v}_C + \mathbf{v}_C\cdot\nabla\mathbf{v}_T) = 0, \tag{3c}$$

$$\frac{\partial p_C}{\partial t} + \left(\frac{NH}{n\pi}\right)^2\nabla\cdot\mathbf{v}_C + \mathbf{v}_T\cdot\nabla p_C = 0. \tag{3d}$$

We nondimensionalized the above equations as follows: The horizontal coordinate $\mathbf{x} = (x, y)$ was scaled using the deformation length $L_D = (NH/\pi f)$, the vertical coordinate z by H, the depth of the ocean, and time t using the inertial time scale, $1/f$. An arbitrary flow velocity scale, U, was chosen as the velocity scale for both barotropic and baroclinic flow. The scale for both barotropic and baroclinic pressure was chosen as fUL, based on the geostrophic balance condition. After applying these scalings, we take the curl of the barotropic equation in (3) to get an evolution equation for $\zeta_T = \nabla\times\mathbf{v}_T$. Additionally, we rescale p_C as $\mathrm{Bu}p_C$ to get the final model in nondimensional form as used in Thomas and Vishnu (2022):

$$\frac{\partial \zeta_T}{\partial t} + \mathrm{Ro}\nabla\times[\mathbf{v}_T\cdot\nabla\mathbf{v}_T + \mathbf{v}_C\cdot\nabla\mathbf{v}_C + (\nabla\cdot\mathbf{v}_C)\mathbf{v}_C] = -\nu\Delta^8\zeta_T, \tag{4a}$$

$$\frac{\partial \mathbf{v}_C}{\partial t} + \hat{\mathbf{z}}\times\mathbf{v}_C + \mathrm{Bu}\nabla p_C + \mathrm{Ro}(\mathbf{v}_T\cdot\nabla\mathbf{v}_C + \mathbf{v}_C\cdot\nabla\mathbf{v}_T) = -\nu\Delta^8\mathbf{v}_C, \tag{4b}$$

$$\frac{\partial p_C}{\partial t} + \nabla\cdot\mathbf{v}_C + \mathrm{Ro}\mathbf{v}_T\cdot\nabla p_C = -\nu\Delta^8 p_C. \tag{4c}$$

Above, we added hyperdissipative terms on the right-hand side to obtain a broader inviscid inertial range and to ensure that energy dissipation is confined to the grid scale, where $\Delta = (\partial^2/\partial x^2) + (\partial^2/\partial y^2)$. The Rossby number $\mathrm{Ro} = U/(Lf)$, while $\mathrm{Bu} = 1/n^2$ is the Burger number. In this work, we will vary Ro from asymptotically small to $O(1)$ values, while $\mathrm{Bu} \ll 1$, since we will be examining interactions between high-baroclinic-mode near-inertial waves (NIWs) and the balanced flow.

Notice that taking curl of the barotropic evolution equation in (3) eliminates spatially homogeneous inertial oscillations in the barotropic mode. All the results presented below were obtained using numerical integrations of (4). Additionally, we performed selected integrations using (3) incorporating similar dissipation terms as in (4). These experiments led to similar

results to those obtained using (4), with the inertial oscillations in the barotropic mode behaving passively with no noticeable changes induced in energy transfers or other statistics.

In the absence of dissipative operators, (4) conserves energy given by

$$E = \int_D \left(\frac{1}{2}\mathbf{v}_T{}^2 + \frac{1}{2}\mathbf{v}_C{}^2 + \frac{1}{2}\mathrm{Bu}p_C{}^2\right)d\mathbf{x}. \tag{5}$$

The first term above corresponds to the barotropic energy E_T, while the sum of the remaining terms corresponds to the baroclinic energy E_C. The energy conservation can be derived by multiplying (4a) by $-\psi_T$, taking the dot product of (4b) with $\mathbf{v}_C$, multiplying (4c) by $\mathrm{Bu}p_C$, summing up the three equations, and integrating over the domain (D) assuming no boundary flux contributions.

Although we use the two-vertical-mode model [(4)] for this study, it is important to note that this being a reduced model, it will miss some of the features seen in the three-dimensional Boussinesq equations. For example, the two-vertical-mode model cannot capture a forward cascade involving multiple baroclinic modes due to its reliance on a single baroclinic mode. Additionally, the model is derived assuming hydrostatic balance, implying that we will miss nonhydrostatic dynamics. Despite such shortcomings, past studies have found similar features in this model and more complex three-dimensional models. For example, Thomas and Daniel (2020) found similar turbulent energy transfers between NIWs and balanced flows in a wave-dominated regime integrating the three-dimensional nonhydrostatic Boussinesq equations to those seen in the two-vertical-mode model study of Thomas and Arun (2020). Similarly, Thomas and Vishnu (2022) found several features of high Rossby number turbulent flows to be qualitatively similar to those seen in the ocean-model-based study of Capet et al. (2008) and oceanic observations detailed in Shcherbina et al. (2013). The two-vertical-mode model has also been used to capture several realistic features of atmospheric flows (Frierson et al. 2004; Pauluis et al. 2008; Stechmann and Majda 2006). In view of these past studies, we will use this model to study the disintegration of coherent barotropic vortices by baroclinic inertial oscillations in this work, with the expectation that the results at least qualitatively match those that would follow from more complex models.

3. Numerical integration details and initialization

We generated different flows by numerically integrating (4) in a doubly periodic domain $[0, 2\pi]^2$ using a two-thirds dealiased Fourier pseudospectral solver with 1152^2 grid points. This sets the maximum wavenumber in each direction as $k_{\max} = (1152/2) \times (2/3) = 384$ after dealiasing. Spatial convergence was checked by using higher resolution for specific flows, especially the higher Rossby number flows, and ensuring that the solutions did not change at higher spatial resolution.

We time stepped the equations using a fourth-order Runge–Kutta method. Time step had to change for different Rossby number flows. All the flows were generated using one of the three time steps: 0.01, 0.005, and 0.001. Lower Rossby number flows used 0.01, while intermediate Rossby number flows needed a time step of 0.005. The $O(1)$ Rossby number flows needed 0.001 as the time step. The appropriate time step was obtained by trial and error, starting with 0.01 and gradually decreasing it until the solutions were insensitive to a further decrease in the time step.

For each integration, we initialized Gaussian vortices by setting $\zeta_T = \alpha e^{-\beta|\mathbf{x}-\mathbf{x}_0|^2}$, where α and β are constants corresponding to the strength and size of the vortex, respectively. The vortex center was set as $\mathbf{x}_0 = (\pi, \pi)$, which is the center of the domain. We also chose $\beta = 2$, which led to vortices that were confined to our domain. Since the barotropic flow is divergence free, ζ_T can capture the full barotropic flow. Specifically, ζ_T can be written in terms of the barotropic streamfunction ψ_T as $\zeta_T = \nabla \times \mathbf{v}_T = \Delta\psi_T$. Thus, once the barotropic vorticity is prescribed, the barotropic velocity fields are obtained. A positive choice for α led to cyclones, while a negative choice led to anticyclones. To obtain unit barotropic energy initially, i.e., $E_T(t = 0)$, we chose $|\alpha| = 2.44$ for all cases. In all experiments, we used Gaussian vortices of unit initial energy.

We initialized the baroclinic flow as $\mathbf{v}_C = (c, 0)$. This initialization excites inertial oscillations of the form $\mathbf{v}_C = c(\cos t, -\sin t)$ based on the linear equations. From the baroclinic flow, we calculated the baroclinic energy, which depends on c. We set c so as to generate regimes with different initial energy ratios, $(E_C/E_T)_{t=0}$. We varied Ro from 0.1 to 1 with increments of 0.1. For each Ro, we used different c to get different initial baroclinic-to-barotropic energy ratio cases. For all cases, we set $\mathrm{Bu} = 0.01$, which in turn fixes $n = 10$; i.e., the baroclinic mode under consideration is 10. We numerically integrated the equations up to $t = 300$ in all regimes and used these data to explore vortex disintegration.

We used a periodic domain, and stronger interactions are expected in this setting that do not allow fast flow components to propagate away. In this sense, the energy transfers and dissipation we find may be considered an upper bound. On the other extreme, we could consider unbounded domains, where flow dynamics can escape by propagating away and, therefore, energy transfers and dissipation would be much lower than what we discuss below. The real ocean has a broad distribution of eddies and waves interacting with each other in addition to persistent wind and other forcings that energize the two kinds of motions. These scenarios may be qualitatively better represented by a periodic setting, where interactions go on for much longer, than an unbounded domain kind of setup, where interactions die out quickly.

4. Characterizing vortex disintegration using enstrophy fraction

Before examining inertial oscillations perturbing the coherent eddy fields, we first initialized barotropic Gaussian vortices and integrated (4) up to $t = 300$ without initializing baroclinic fields. The final state of a Ro = 1 anticyclonic vortex is shown in Fig. 1a, while Fig. 1b shows the difference in vorticity between the final and initial states. Notice that the vortex is intact in its initial form, although weak disturbances of the order of $O(10^{-3})$ can be seen in the difference plot in Fig. 1b. Similar results were seen for all vortex integrations

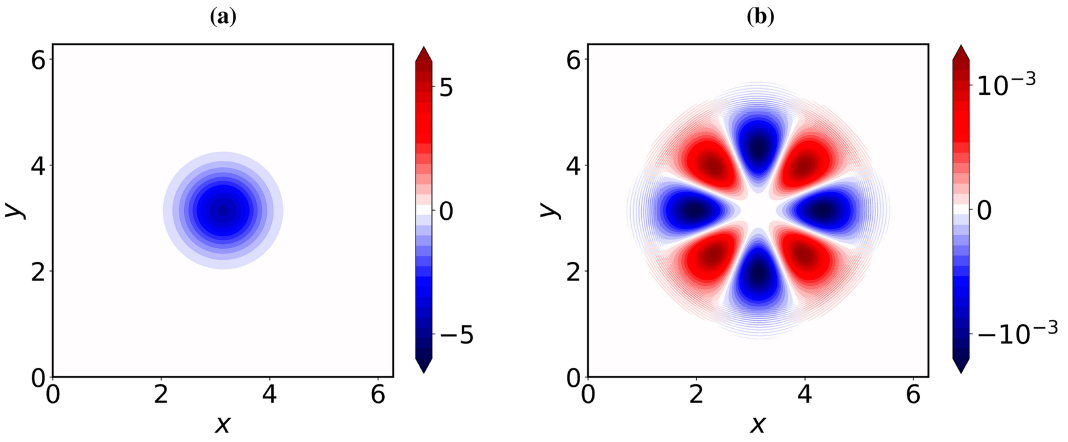

FIG. 1. Physical structure of a flow with Ro = 1.0 and no inertial oscillation initialization. (left) Barotropic vorticity at $t = 300$. (right) Difference in barotropic vorticity field between $t = 300$ and $t = 0$.

without the baroclinic flow. These integrations, without adding inertial oscillations, were important to ensure that in the absence of inertial-oscillation disturbances, the vortices were stable and retained their initial structure, albeit weak perturbations that appear in the flow. We used the state at $t = 300$ as the initial condition and introduced inertial oscillations of different strengths on top of that to see how they can affect the eddy field.

We added baroclinic inertial oscillations of varying energy levels on top of the barotropic eddies to generate 640 regimes in total: 320 each with anticyclonic vortex initialization and with cyclonic vortex initialization. These cases are shown with a scatterplot in the Rossby number–energy ratio space in Fig. 2a, with the regimes being denoted with black dots as markers.

Given the barotropic vorticity at a given time, $\zeta_T(\mathbf{x}, t)$, we take its Fourier transform along the x and y directions and bin over the wavenumbers to obtain $\hat{\zeta}_T(k, t)$, where $k = \sqrt{k_x^2 + k_y^2}$ with k_x and k_y being the wavenumbers along the x and y directions, respectively. The enstrophy associated with a specific wavenumber k is then $|\hat{\zeta}_T(k, t)|^2$. Using this, we define the ratio of enstrophy at wavenumbers greater than a specific wavenumber k_0 to the net enstrophy as

$$\mathscr{E}(t) = \frac{\sum_{k>k_0} |\hat{\zeta}_T(k, t)|^2}{\sum_{k} |\hat{\zeta}_T(k, t)|^2}. \tag{6}$$

The enstrophy ratio, $\mathscr{E}$, is a time-evolving quantity and informs us about the fraction of enstrophy associated with scales below $1/k_0$. Hereafter, we set $k_0 = 10$, helping us estimate the fraction of enstrophy associated with scales one decade below the domain scale, $k = 1$.

For all the coherent vortices used to initialize the flow along with inertial oscillations, such as the vortex state shown in Fig. 1, for example, $\mathscr{E} = 1.50 \times 10^{-11}$, indicating that almost all the enstrophy is contained in the first decade of scales. Scales $k > 10$ have negligible initial enstrophy for the coherent vortex we use. Interactions with the inertial oscillations distort the vortex and generate smaller-scale features, eventually with a significant fraction of enstrophy being transferred to smaller scales. This leads to $\mathscr{E}$ increasing from its initial value, and we define $\mathscr{E}^*$ as the maximum value of $\mathscr{E}$ attained during the flow evolution. We then define vortex disintegration to be the case when the enstrophy ratio $\mathscr{E}^*$ reaches 95% or above, i.e., $\mathscr{E}^* \geq 0.95$ for disintegrating vortices.

For all the flows we generated shown in Fig. 2a, we computed $\mathscr{E}^*$. This data is then plotted after applying a cubic interpolation to get the bottom row of Fig. 2, with the left and right panels being for anticyclones and cyclones, respectively. Notice that low Rossby number and low energy ratio result in low $\mathscr{E}^*$ blue regions, while increasing these variables takes us through green, yellow, and eventually red regions with high values of $\mathscr{E}^*$. For both cases, we see that vortices disintegrate at lower energy ratios with increasing Rossby number. The 95% contour line of $\mathscr{E}^*$ is highlighted with a broken white line in each panel. These lines are further plotted in Fig. 3a. Notice that anticyclone curve, in general, lies slightly to the left of cyclone curve, indicating that anticyclone disintegration can take place at relatively lower Rossby number for a given energy ratio than cyclone disintegration.

The bottom row of Fig. 3 shows the effect of changing $\mathscr{E}^*$, with blue and red curves corresponding to $\mathscr{E}^* = 93\%$ and $\mathscr{E}^* = 97\%$. Decreasing the enstrophy ratio threshold to define vortex disintegration moves the new curve to the left of the black curve with the 95% threshold. On the other hand, increasing the threshold to 97% moves the curve rightward.

An interesting observation from the bottom row of Fig. 3 is that the curves corresponding to $\mathscr{E}^* = 93\%$ and $\mathscr{E}^* = 97\%$ migrate more from the $\mathscr{E}^* = 95\%$ curve at higher Rossby numbers, while the three curves almost coincide at low Rossby numbers. This feature may be attributed to the higher level of ruggedness of balanced flows at low Rossby numbers, as discussed in the introduction. A high level of unbalanced energy is required to disintegrate and dissipate balanced flows at low Rossby numbers (also see different studies on this reviewed in Thomas 2023). Slightly increasing the energy level of unbalanced flow does not change these dynamics. On the other hand, a low level of unbalanced energy can breakdown

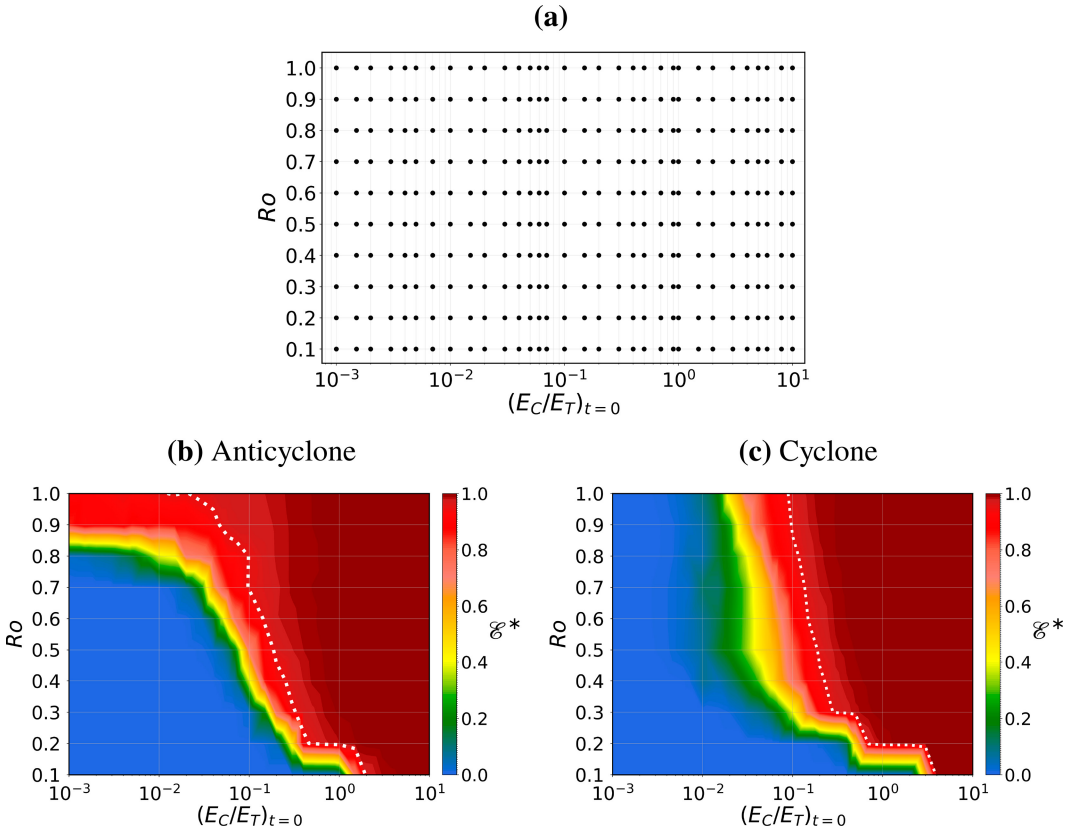

FIG. 2. (a) The flow regimes on the Rossby number–energy ratio diagram. The contour plots of $\mathscr{E}^*$ for (b) anticyclonic and (c) cyclonic vortices. The broken white lines correspond to $\mathscr{E}^* = 95\%$.

and dissipate balanced flows at higher Rossby numbers (Capet et al. 2008; Thomas and Vishnu 2022). As a result of this, small changes in the threshold for disintegrating balanced flow can move the critical curves more in the higher Rossby number regime, as seen for the $\mathscr{E}^* = 93\%$ and $\mathscr{E}^* = 97\%$ curves in Fig. 3.

As we shall see by examining physical structures below, vortex disintegration is characterized by a significant distortion of the original coherent vortex with the generation of a lot of small-scale structures. Such an extreme change in the flow field can be captured by different metrics, with the enstrophy ratio we used being a specific one. In the appendix, we show that we can get similar curves as $\mathscr{E}^* = 95\%$ lines above by setting a threshold for a different metric: azimuthal vorticity distribution.

5. Physical structure of disintegrating vortices

We will now discuss the physical structures of vortices. First, we will look at six energy ratio cases corresponding to Ro = 0.5, these being highlighted with the black dots in Fig. 3a. As seen from the figure, three cases are before the vortex disintegration curve, one point is immediately to the right of the disintegration curve, and two points are further to the right of the curve.

Figures 4a–f show the physical structure of anticyclones for the six cases mentioned above. On top of each panel, we have the energy ratio, time, and $\mathscr{E}$. For the three cases where the vortex did not disintegrate, we have the physical structure at $t = 300$, this being shown in the first row of Fig. 4. Notice that as we move from Figs. 4a–c, we see a progression in small-scale vorticity structures and erosion of the coherent vortex. For the remaining three cases, we have the vortex structure immediately after the enstrophy ratio exceeds 95%, i.e., right after vortex disintegration took place, and these cases are shown in the second row of Fig. 4. For these vortices, we see a lot more fine-scale vorticity structures, making it difficult to identify the initial coherent vortex structure.

Features similar to above are seen for the cyclonic vortex shown in the last two rows of Fig. 4. In Figs. 4g–i, where the vortex does not disintegrate based on our criterion of enstrophy ratio, we see a coherent vortex resembling the initial vortex along with some small-scale vorticity structures in the domain. On the other hand, vortex-disintegrating cases shown in Figs. 4j–l show a lot more fine-scale vorticity structures along with significant distortion of the initial vortex.

We will now compare the spatial structure of the vortices with the Okubo–Weiss (OW) parameter (Okubo 1970; Weiss 1991). The OW parameter is usually used to identify coherent vortices in oceanographic flows at meso- and submesoscales (Provenzale 1999; Shcherbina et al. 2013; Chelton et al. 2007) and is defined as

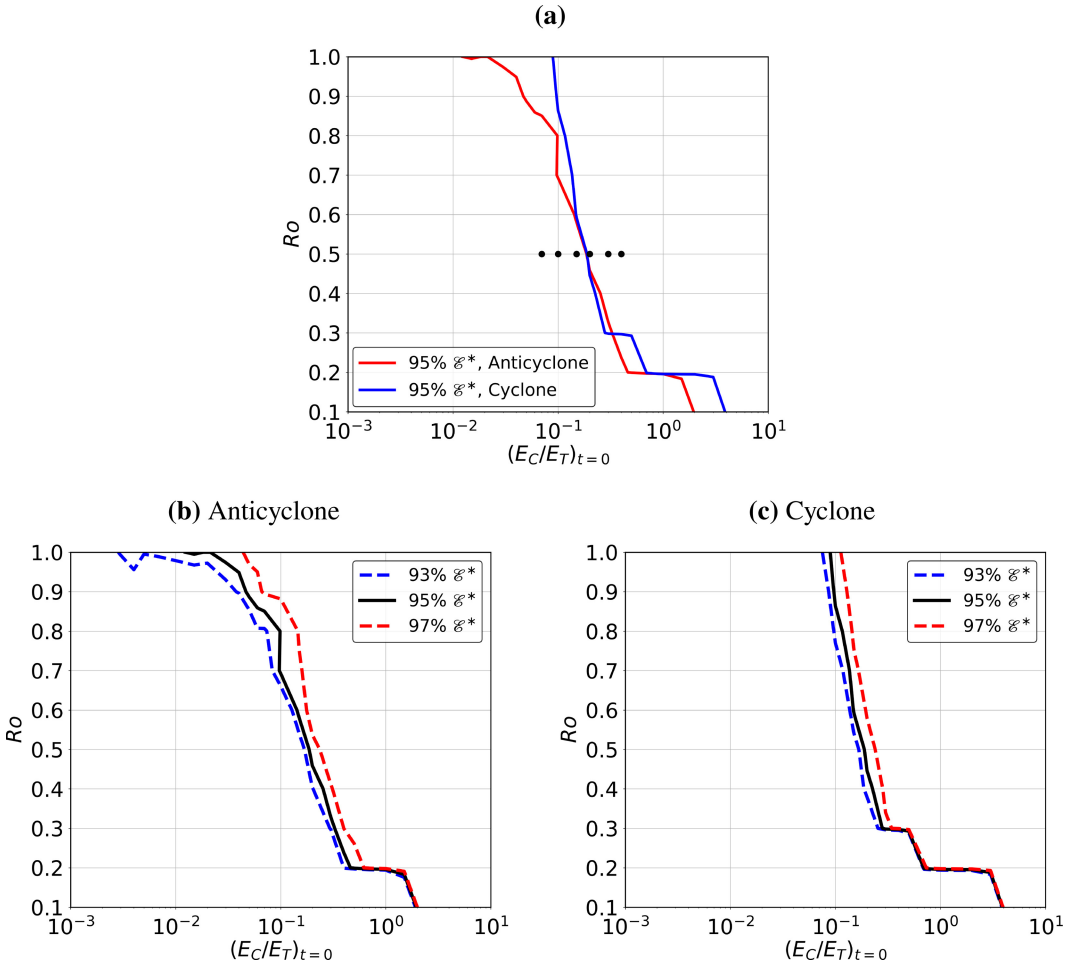

FIG. 3. (a) The vortex disintegration curves for anticyclone (red) and cyclone (blue) with $\mathscr{E}^* = 95\%$. Black dots indicate six cases with Ro = 0.5 whose physical structures are given in Fig. 4. (b),(c) The changes in vortex disintegration curves if the threshold is changed to 93% and 97%. Panel (b) is for anticyclone while (c) is for cyclone.

$$\mathrm{OW} = \sigma^2 - \zeta^2, \tag{7}$$

where $\sigma^2 = s_n^2 + s_s^2$ is the squared strain magnitude, with $s_n = \partial u/\partial x - \partial v/\partial y$ being the normal strain and $s_s = \partial v/\partial x + \partial u/\partial y$ being the shear strain, while $\zeta = \partial v/\partial x - \partial u/\partial y$ is the vorticity. The OW parameter helps us separate regions of strain dominance, OW > 0, from vorticity-dominant regions, OW < 0. Coherent vortex containing fields will have OW < 0 in the vortex and OW > 0 outside the vortex, i.e., vortex cores form vorticity-dominant regions, while the outside regions are strain-dominant.

Figure 5 shows barotropic vorticity fields for Ro = 0.5 and $(E_C/E_T)_{t=0} = 6$, a case where both anticyclone and cyclone disintegrate. Figures 5a–h show the disintegration phases of the anticyclone. The disintegration of an anticyclone begins with the stretching of the initial vortex as seen in Fig. 5b. The vortex core stretches and then gets split into two in Fig. 5c. The two vortex cores thus formed orbit around each other in a clockwise direction, which can be observed from comparing Figs. 5b–d. Figure 5d shows red high-intensity filaments in vorticity along the edge of the two cores. These filaments are followed by the formation of fine-scale dissipative structures that start to spread over a larger area, as seen in Fig. 5e. From Figs. 5f–h, it can be seen that the fine-scale structures expand and engulf the entire vortex.

Multiple past studies have examined the stability of coherent vortices in the presence of external perturbations using a variety of settings, such as the two-dimensional vorticity equation, quasigeostrophic equation, and Boussinesq equations (Mariotti et al. 1994; Sutyrin 2019; Viúdez 2021; Flierl 1988; Brunner-Suzuki et al. 2012). Irrespective of the model used, these studies also find vortex filaments being ejected from the coherent vortex before the primary vortex splits into smaller vortices. Figures 5a–d resemble the dynamics seen in these past studies using different models.

The last two rows of Fig. 5 show the OW parameter corresponding to the vorticity fields shown in the first two rows of the figure. Observe that as the vortex disintegrates, the initial coherent vortex characterized by OW < 0 in Fig. 5i transitions into a strain-dominant region with OW > 0. Initially,

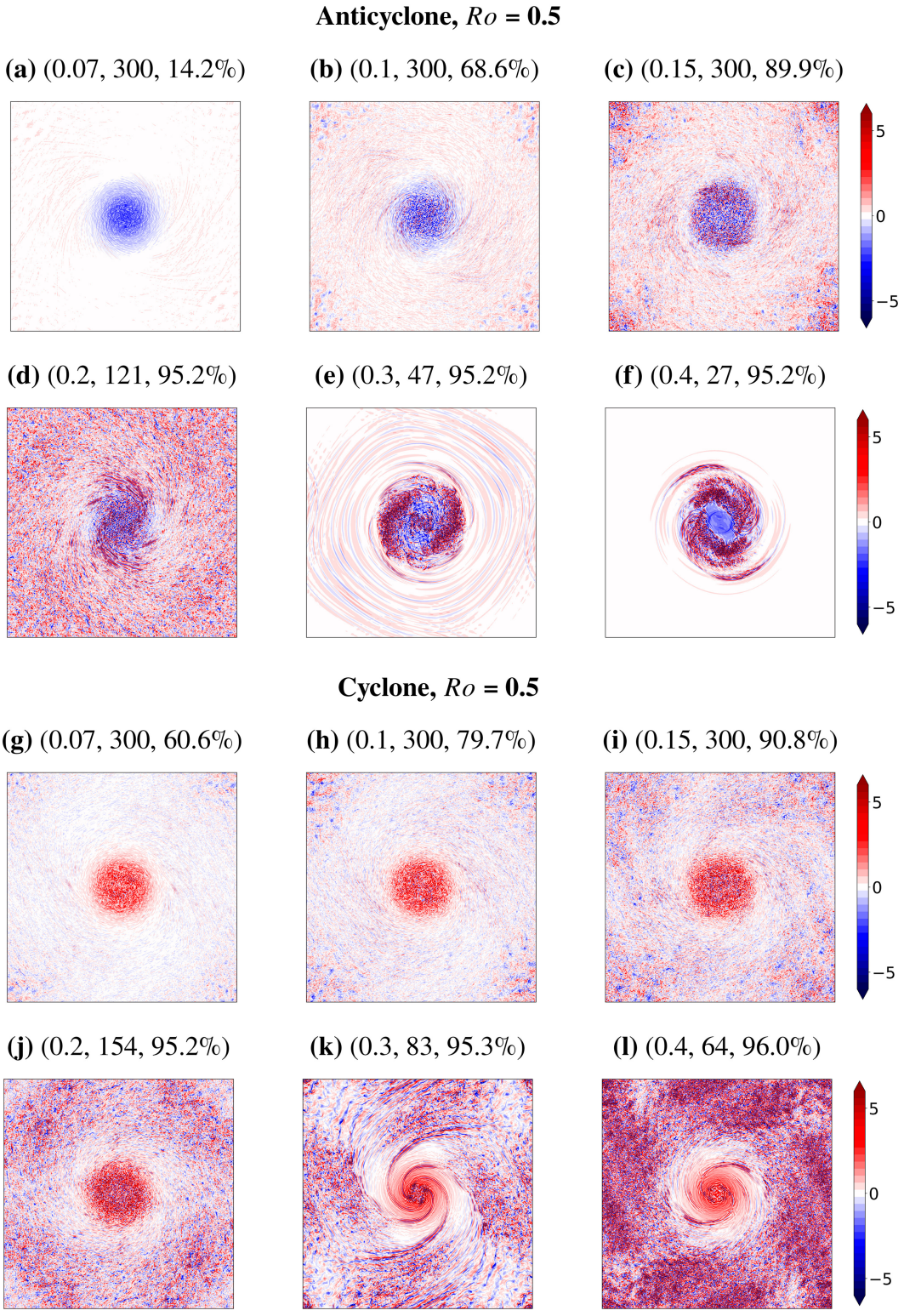

FIG. 4. Vorticity fields for Ro = 0.5 and the six energy ratio cases marked by black dots in Fig. 3a. (a)–(f) Anticyclone; (g)–(l) cyclone. Above each panel, we have written a triad of numbers indicating energy ratio, time, and enstrophy fraction.

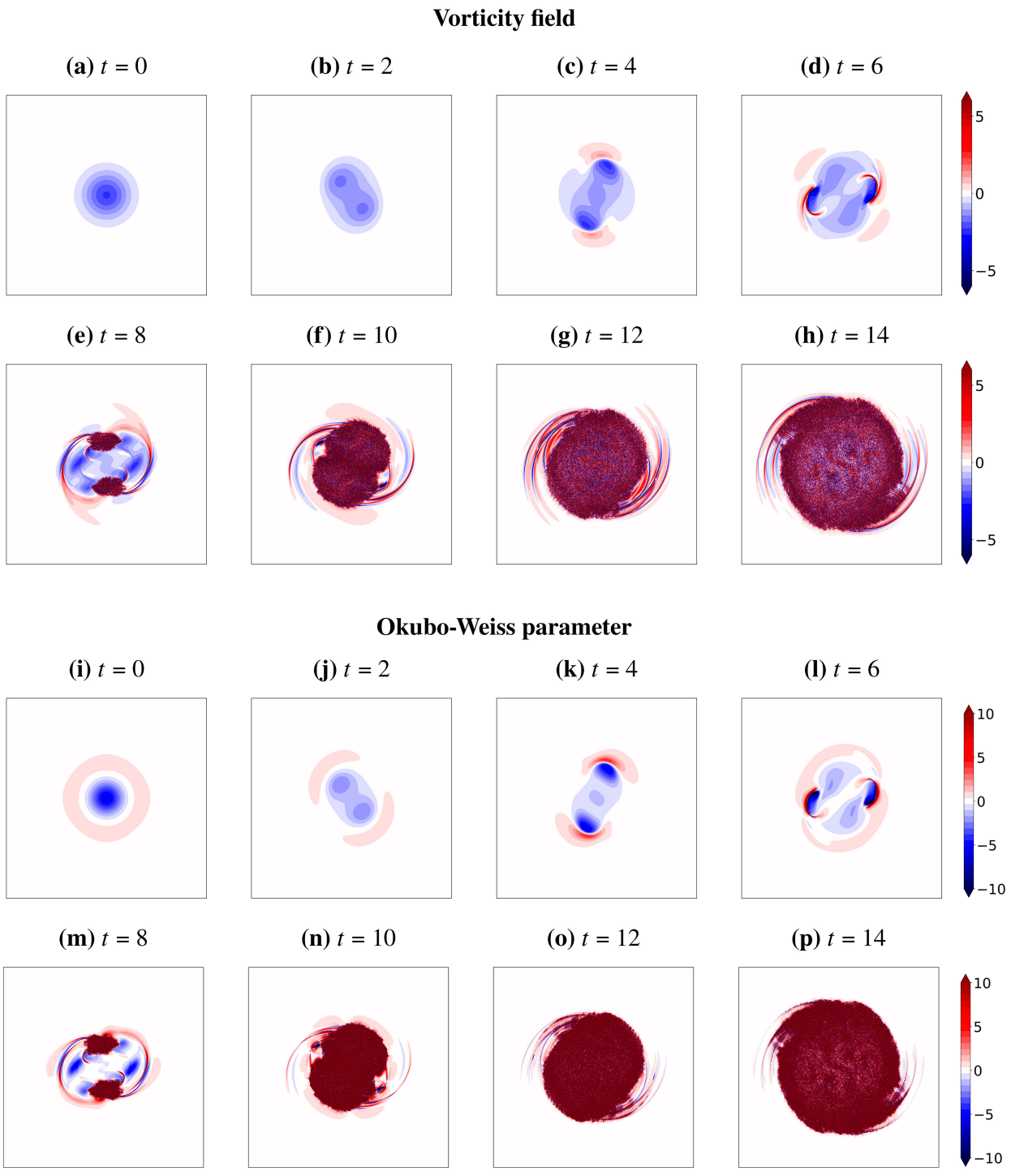

FIG. 5. (a)–(h) The barotropic vorticity field at different times. Anticyclone for Ro = 0.5 and $E_C/E_T = 6$ is shown. (i)–(p) The OW parameter for the same times.

strain-dominant regions lie outside the vortex core, although with time they enter the vortex core and convert the entire vortex core into a strain-dominant region. Vortex disintegration therefore transforms the vortex core from OW < 0 region to an OW > 0 region.

Compared to anticyclones, we found multiple qualitative differences in the way cyclones disintegrate, as shown in Figs. 6a–h. In the early stages, from Figs. 6b–d, we see vortex spirals ejecting from the initial core. In Figs. 6e and 6f, it can be observed that some of these spirals detach from the core

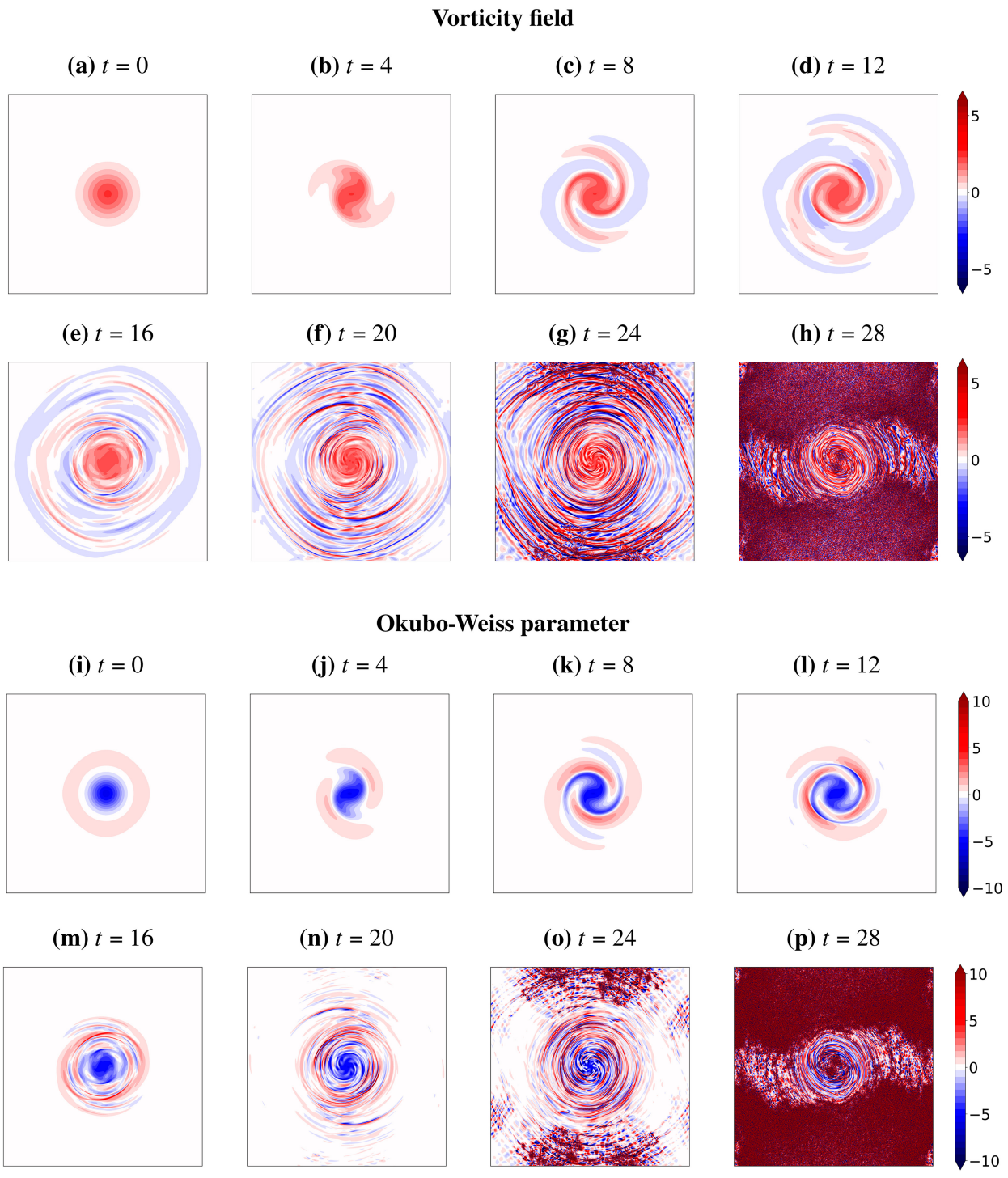

FIG. 6. (a)–(h) The barotropic vorticity field at different times. Cyclone for Ro = 0.5 and $E_C/E_T = 6$ is shown. (i)–(p) The OW parameter for the same times.

and form concentric rings around the vortex. The formation of small-scale structures begins from these rings, which can be seen from Fig. 6g. The small-scale structures then spread across and fill the whole domain by Fig. 6h. Interestingly, the formation of spirals is something that was seen only in cyclones, while splitting of the vortex core into two parts was exclusive to anticyclones. It can also be noted that the small-scale structures are formed much earlier in the anticyclone,

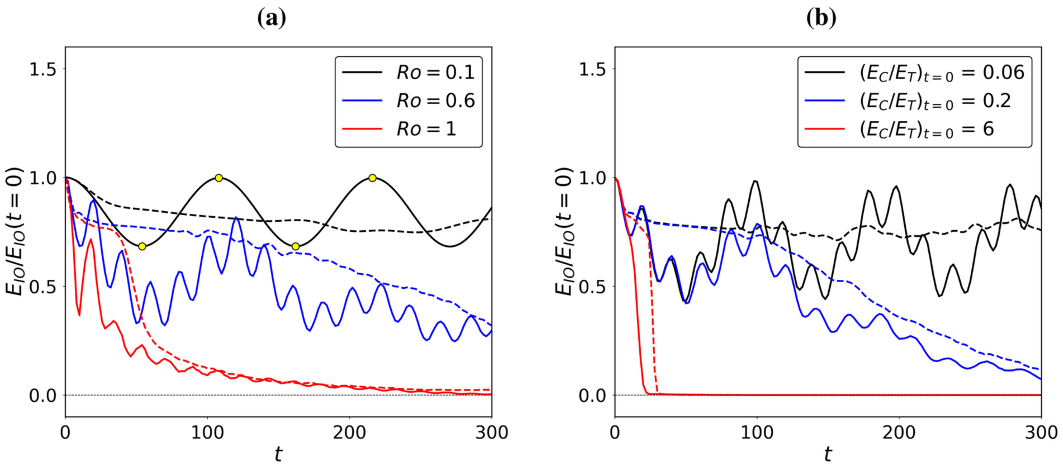

FIG. 7. E_{IO}/E_{IO} ($t = 0$) (a) for different Ro and $(E_C/E_T)_{t=0} = 0.1$ and (b) for different $(E_C/E_T)_{t=0}$ and Ro = 0.5. Solid lines are for anticyclones, while dashed lines are for cyclones.

at $t = 8$ in Fig. 5e, compared with the cyclone, at $t = 24$ in Fig. 6g.

Examining the OW parameter, shown in the last two rows of Fig. 6, we see that vortex disintegration transforms the vortex-dominant OW < 0 region into a strain-dominant OW > 0 region, this being similar to the anticyclone case. The spirals are strain-dominant regions, and these structures enter the vortex core, followed by the formation of fine-scale dissipative structures in the vortex core.

As seen from Fig. 5, sharp filaments in anticyclonic vortices form in the early stages, followed by their conversion into fine-scale dissipative structures that spread across the entire vortex. The initiation of the vortex disintegration was seen to start with the filament formation. Lowering Rossby number was seen to bring the initial filaments closer to the vortex core while increasing the Rossby number moved the initial filaments away from the vortex core. Interestingly, in some sense, the opposite behavior was seen for cyclones. Cyclonic vortices were seen to develop fine-scale spiral structures away from the vortex core at low Rossby numbers, while the spiral fine-scale features were seen to be located closer to the core at higher Rossby numbers. These changes were qualitatively similar with increasing energy ratio: Anticyclonic vortices' filaments moved away from the core, while cyclonic spirals moved closer to the core with increasing energy ratio.

6. Inertial oscillations' dynamics

The above description was for the barotropic flow perturbed by the baroclinic field. We will now look at the dynamics of inertial oscillations in the baroclinic field as a function of Rossby number and energy ratio. Although we initialized spatially homogeneous inertial oscillations, their interaction with the eddy can generate spatially inhomogeneous NIWs, whose frequency might not coincide exactly with the inertial frequency. This process can result in inertial oscillations transferring their energy to the other flow components. To see this feature, from the baroclinic flow we isolated the spatially homogeneous inertial oscillation component, $\mathbf{v}_{IO}$, by a horizontal averaging operation and computed the associated kinetic energy as

$$E_{IO}(t) = \int_D \frac{1}{2}\mathbf{v}_{IO}^2 d\mathbf{x}. \tag{8}$$

The time evolution of inertial oscillations' kinetic energy indicated interesting features when comparing anticyclones and cyclones. Figure 7 shows E_{IO} normalized by its initial value for cases with varying Rossby numbers (left panel) and energy ratios (right panel). In the left panel, which shows the cases with $(E_C/E_T)_{t=0} = 0.1$, the black solid line corresponds to an anticyclone with Ro = 0.1. Notice that the curve oscillates with time. This is a case where the vortex does not disintegrate. The blue solid line in Fig. 7a corresponds to an anticyclone with Ro = 0.6, where the vortex is approaching the threshold $(E_C/E_T)_{t=0}$ needed to disintegrate. In this case, we see an oscillatory decay of the amplitude of the oscillation of E_{IO} with time. As we increase Ro further to 1, the vortex now disintegrates under $(E_C/E_T)_{t=0} = 0.1$. As a result, E_{IO} shown with the red curve in Fig. 7a tends to zero. Therefore, when an anticyclone has Ro and $(E_C/E_T)_{t=0}$ close to the region where the vortex is expected to disintegrate, E_{IO} oscillates and decays, gradually going to zero as the vortex disintegrates. Contrary to the anticyclones, the dashed lines in Fig. 7a corresponding to cyclones show no oscillations. The black dashed line corresponding to a cyclone with Ro = 0.1 has a slight dip initially and then maintains its value. For the cyclone with Ro = 0.6, shown with the dashed blue line, we see a gradual decay in E_{IO}, but without oscillations. In the red dashed curve, which is for a cyclone with Ro = 1, E_{IO} decays to zero, similar to the anticyclone. Thus, although no oscillations are seen, E_{IO} of the cyclone also gradually decays to zero as the vortex disintegrates.

As is well known from simple theoretical models, complex ocean models, and in situ observations, NIWs are trapped by anticyclonic vortices and are repelled by cyclonic vortices (Danioux et al. 2015; Thomas et al. 2017; Lee and Niiler 1998;

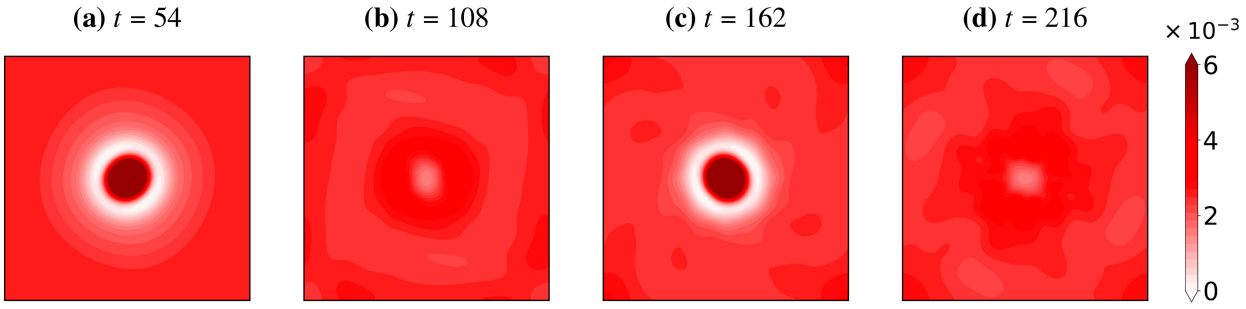

FIG. 8. (a)–(d) Baroclinic energy density fields for Ro = 0.1 and $(E_C/E_T)_{t=0}$ = 0.1. The times corresponding to (a)–(d) are marked as yellow dots in Fig. 7a.

Elipot et al. 2010). Additionally, in low Rossby number regimes when interacting with coherent vortices, NIWs trapping can be periodic in nature, with the wave energy increasing and then decreasing periodically. This feature has been noted in past studies; see, for example, Figs. 4 and 5 in Thomas et al. (2017). We did see a similar feature in the physical structure of the baroclinic flow. Figure 8 shows physical structures of baroclinic energy, i.e., the sum of the last two terms inside the integral in (5), corresponding to the time instants marked with yellow dots in Fig. 7a. This is a case of an anticyclone where the vortex does not disintegrate, with Ro = 0.1 and $(E_C/E_T)_{t=0}$ = 0.1. The NIWs are periodically trapped in and released from the vortex cores as can be seen in Figs. 8a–d. The trapped energy in the vortex core is at its maximum in Figs. 8a and 8c, which corresponds to the troughs in Fig. 7a. At times corresponding to the crests in Fig. 7a, the trapped energy in the vortex core is at its minimum, as seen in Figs. 8b and 8d. The time period of the oscillation is close to 108, which is about 17 times the inertial time period of 2π.

The periodic trapping and relieving of NIWs from vortex cores at low Rossby numbers led to minimal loss of inertial oscillation energy to other modes of the flow, leading to an almost absence of decay in the inertial oscillation energy as seen in the solid black curve in Fig. 7a. Increasing Rossby number, however, generates fine-scale flow features along with the conversion of inertial oscillation energy to other modes. Past studies have found this behavior while exploring inertial oscillations interacting with eddy fields: Finer-scale features in the eddy will lead to more intense interactions and generate finer-scale wave fields that can dissipate quickly (see discussions in Danioux et al. 2015; Thomas et al. 2017). This leads to the oscillatory decay of E_{IO} with time seen in the blue and red curves in Fig. 7a.

Figure 7b shows an example set of cases where the energy ratio is varied for Ro = 0.5. Despite quantitative differences, we see qualitatively similar features to those seen in Fig. 7a. Notably, for anticyclones, we see oscillatory behavior with no decay at low energy ratio (solid black), oscillatory behavior with energy decay on increasing energy ratio (solid blue), and a sharp drop in energy at high energy ratio (sold red). On the other hand, no oscillations are seen in the case of cyclones (dashed black, blue, and red curves). Therefore, as in the previous figures, we see that increasing energy ratio plays a qualitatively similar role to increasing Rossby number.

7. Barotropic–baroclinic energy transfers, flux, and dissipation

Having looked at inertial oscillations' energetics above, we will now look at the barotropic and baroclinic energy changes. Multiplying (4a) by ψ_T and integrating over the domain gives us the evolution equation for the barotropic energy, E_T. Similarly, summing the dot product of (4b) with $\mathbf{v}_C$ and the product of (4c) with $\mathrm{Bu}p_C$, and integrating the sum over the domain gives us the evolution equation for baroclinic energy, E_C. These are

$$\frac{dE_T}{dt} = T_{TC} - D_T, \tag{9a}$$

$$\frac{dE_C}{dt} = T_{CT} - D_C. \tag{9b}$$

Above, T_{TC} is the baroclinic-to-barotropic energy transfer term and is the domain integral of the product of ψ_T and the nonlinear terms in (4a), i.e., all the terms multiplied by Ro. A positive value for this term implies that the barotropic mode is gaining energy from the baroclinic mode and vice versa if the term is negative. The barotropic dissipation D_T is the domain integral of the product of ψ_T with the hyperdissipative term in (4a) and represents barotropic energy dissipation. Similarly, T_{CT} above is the barotropic-to-baroclinic energy transfer term and is the domain integral of the sum of the dot product of $\mathbf{v}_C$ with the nonlinear terms in (4b) and the product of $\mathrm{Bu}p_C$ with the nonlinear terms in (4c). Since (4) conserves energy given in (5), energy gained by barotropic mode must be lost by the baroclinic mode and vice versa. This gives us $T_{CT} = -T_{TC}$. Finally, D_C is the baroclinic energy dissipation.

We will examine the energetics from (9) for different cases, but first we show a particular case that demonstrates the qualitative nature of the transfers. In Fig. 9, we highlight an example case, Ro = 0.5 and $(E_C/E_T)_{t=0}$ = 6, the same case whose physical structures were explored in Figs. 5 and 6. Figure 9a shows the fractional change in barotropic and baroclinic energies, Fig. 9b shows the corresponding dissipations, and Fig. 9c shows the energy transfer term, T_{TC}. In Fig. 9a, we see that the barotropic energy (black lines) increases on a short time scale, reaches a maximum, and then slowly decreases, while the baroclinic energy (red curves) drops quickly. Notice that baroclinic energies start to drop right when the barotropic energies start

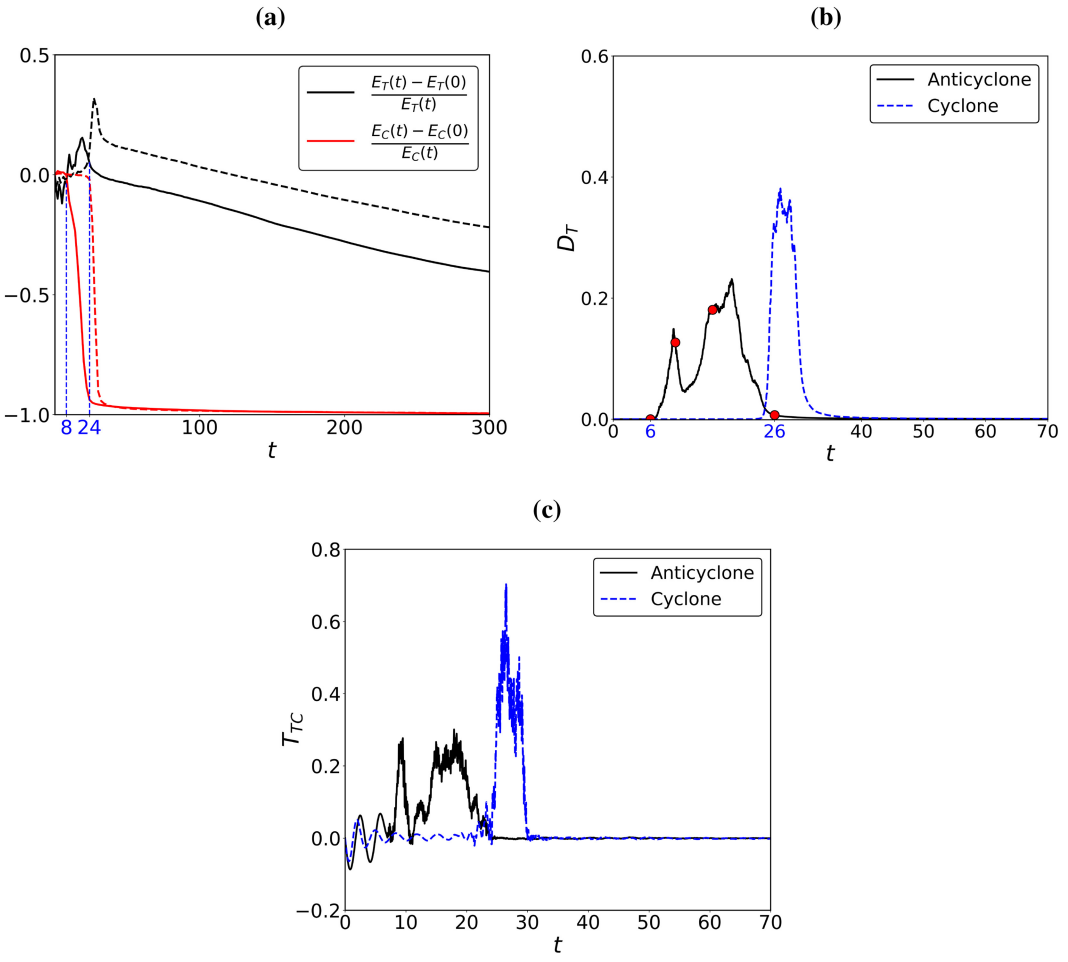

FIG. 9. For the case Ro = 0.5 with initial $E_C/E_T = 6$, the figure shows (a) relative change in barotropic and baroclinic energy, (b) domain-integrated barotropic dissipation, and (c) baroclinic-to-barotropic energy transfer term. In all panels, solid line is used for anticyclone and dashed line for cyclone. In (b), red dots are marked at $t = 6$, 10, 16, and 26 for anticyclone.

the steep rise, and we have marked these times with dashed blue lines in Fig. 9a. The baroclinic energy for the anticyclone starts to drop earlier, at $t = 8$, while that of the cyclone drops a little later, at $t = 24$. Since there is no external energy injection into the system, the barotropic energy should increase as a result of energy transfer from the baroclinic flow, and this is confirmed by Fig. 9a.

From the dissipation curves in Fig. 9b, we see that the solid and dashed curves, corresponding to the anticyclone and cyclone again, are prominent only in a short time window. This indicates that most of the dissipation happens in a short time period. Notice that this window of high D_T starts early and is more spread in time for the anticyclone, while it attains higher magnitudes and lasts for a shorter duration of time for the cyclone. These observations align with our inference from Fig. 5, where we noticed that small-scale dissipative structures appear and spread earlier for the anticyclone than the cyclone. The baroclinic dissipation D_C too had peak values at the same time intervals as those of D_T and is omitted here. The energy transfer term in Fig. 9c is mostly positive, indicating that the barotropic mode is gaining energy from the baroclinic mode. Similar to the dissipation seen in Fig. 9b, we see that the anticyclone has energy transfer spread over a larger time window, while energy transfer for cyclone is more localized in time.

The above analysis reveals that the baroclinic mode containing the near-inertial wave field transfers energy to the coherent vortex as it disintegrates. This feature, of fast waves transferring energy to the vortical field as the later field disintegrates, is a feature seen in some previous studies. For example, Brunner-Suzuki et al. (2012) found that a large-scale internal wave transferred energy to a coherent vortex as it broke up into smaller vortices. Similarly, Thomas and Yamada (2019) found that low baroclinic mode internal waves transferred energy to a turbulent balanced flow, this energy transfer accompanying the generation of finer-scale features of the balanced turbulent flow.

We now split the flow regions into strain-dominant, OW > 0, and vorticity-dominant regions, OW < 0, as before and examine how dissipation and energy transfers behave in these different flow regions. Figure 10 shows these decompositions. From

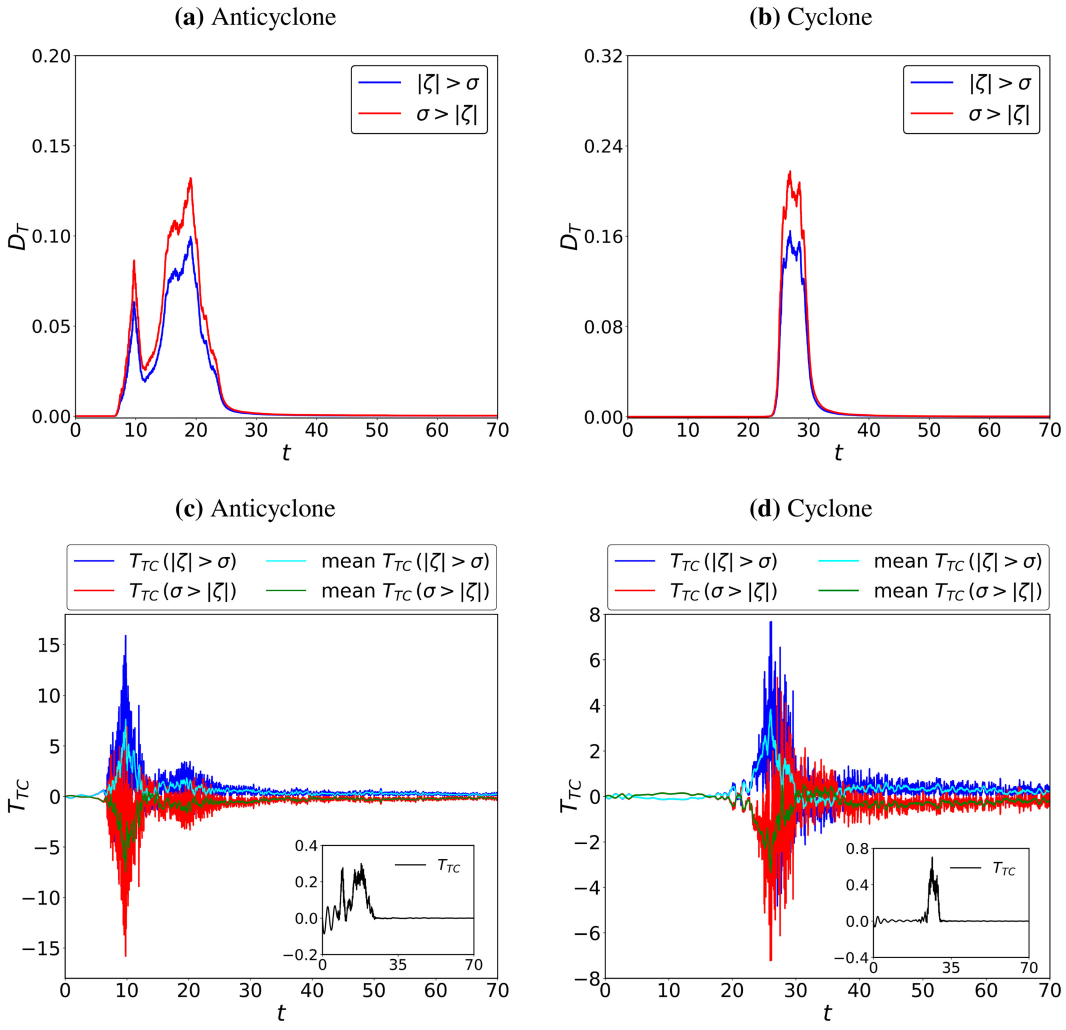

FIG. 10. (top) Domain-integrated barotropic dissipation and (bottom) transfer term T_{TC} for strain- and vorticity-dominated regions, shown separately for (left) anticyclones and (right) cyclones. In the bottom row, light blue and dark green curves are used to indicate running time-averaged transfer curves. All panels correspond to Ro = 0.5 with initial $E_C/E_T = 6$.

the top row of the figure, we see that dissipation is higher in strain-dominant OW > 0 regions than in vorticity-dominant OW < 0 regions for both anticyclones and cyclones. The bottom row of the same figure shows the energy transfer term and its decompositions. Since the transfers in strain-dominant and vorticity-dominant regions fluctuate a lot, running-average mean curves computed using data from 50 time steps are added in the panels. Additionally, the net transfer term is shown in the inset of each panel. From these figures, we see that the barotropic flow is losing energy to baroclinic flow in strain-dominant regions and gaining energy in vorticity-dominant regions. Additionally, we see that the transfers in these individual regions are an order of magnitude higher than the net transfer seen in the inset.

It is interesting to note that some of the above dynamics have been identified in energy transfers diagnosed from oceanic mooring datasets. Jing et al. (2017, 2018) explored inertial oscillations interacting with slow-evolving eddies. They examined the energy transfer terms and checked the transfers in strain-dominant and vorticity-dominant regions. Their datasets revealed that baroclinic inertial oscillations extracted energy from eddies primarily in strain-dominant regions, while vortex dominant regions were associated with less transfer. Of course, these studies were not examining cases where eddies disintegrated, making their setup a bit far from disintegrating vortices' dynamics we are studying. Nevertheless, it is noteworthy that we also see strain-dominant regions being associated with energy extraction by the baroclinic flow containing inertial oscillations.

a. *Energy flux and dissipation during vortex disintegration*

We will now look at the physical structure of energy flux and dissipation during vortex disintegration. To obtain the

flux, we used a spectral filter which filters out large wavenumbers from the field it is applied to. For example, denoting $\mathscr{F}$ and $\mathscr{F}^{-1}$ as the forward and inverse Fourier transform operators, $\hat{\zeta} = \mathscr{F}(\zeta)$ is the Fourier transform of an arbitrary field ζ, and $\tilde{\zeta} = \mathscr{F}^{-1}[\hat{\zeta}(k \le k_L)]$ is the large-scale component of the field ζ, k_L being the filtering wavenumber. $\tilde{\zeta}$, therefore, contains only wavenumbers smaller than the filtering wavenumber k_L. Applying this filter to the governing Eqs. (4a)–(4c) gives us

$$\frac{\partial \tilde{\zeta}_T}{\partial t} + \mathrm{Ro}\nabla \times \left[\widetilde{(\mathbf{v}_T\cdot\nabla\mathbf{v}_T)} + \widetilde{(\mathbf{v}_C\cdot\nabla\mathbf{v}_C)} + \widetilde{(\nabla\cdot\mathbf{v}_C)\mathbf{v}_C}\right] = -\nu\Delta^8\tilde{\zeta}_T, \tag{10a}$$

$$\frac{\partial \widetilde{\mathbf{v}_C}}{\partial t} + \hat{\mathbf{z}}\times\widetilde{\mathbf{v}_C} + \mathrm{Bu}\nabla\widetilde{p_C} + \mathrm{Ro}\left[\widetilde{(\mathbf{v}_T\cdot\nabla\mathbf{v}_C)} + \widetilde{(\mathbf{v}_C\cdot\nabla\mathbf{v}_T)}\right] = -\nu\Delta^8\widetilde{\mathbf{v}_C}, \tag{10b}$$

$$\frac{\partial \widetilde{p_C}}{\partial t} + \nabla\cdot\widetilde{\mathbf{v}_C} + \mathrm{Ro}\widetilde{(\mathbf{v}_T\cdot\nabla p_C)} = -\nu\Delta^8\widetilde{p_C}. \tag{10c}$$

We multiply (10a) with $-\widetilde{\psi_T}$, take the dot product of (10b) with $\widetilde{\mathbf{v}_C}$, multiply (10c) with $\mathrm{Bu}\widetilde{p_C}$, and sum them all up to get the time evolution of the large-scale pointwise energy density, $\tilde{e} = (\widetilde{\mathbf{v}_T}^2 + \widetilde{\mathbf{v}_C}^2 + \mathrm{Bu}\widetilde{p_C}^2)/2$, as

$$\frac{\partial \tilde{e}}{\partial t} + \mathrm{Ro}\widetilde{\mathbf{v}_T}\cdot\nabla\tilde{e} = \nabla\cdot M_1 + \nabla\times M_2 + \nabla\cdot M_3 - \widetilde{\Pi_T} - \widetilde{\Pi_C} - \tilde{d}, \tag{11}$$

where $\tilde{d}$ is the dissipation. The energy transfer terms on the right-hand side of the above equation are

$$M_1 = -\mathrm{Bu}\widetilde{p_C}\,\widetilde{\mathbf{v}_C} + \widetilde{\psi_T}\nabla\widetilde{\frac{\partial\psi_T}{\partial t}} - \frac{1}{2}\mathrm{Ro}\widetilde{\mathbf{v}_T}\widetilde{\psi_T\zeta_T} + \frac{1}{2}\mathrm{Ro}\widetilde{\mathbf{v}_T\mathbf{v}_C}^2 + \mathrm{Ro}\widetilde{\mathbf{v}_T p_C}, \tag{12a}$$

$$M_2 = \mathrm{Ro}\tilde{\psi}_T\left[\widetilde{(\mathbf{v}_T\cdot\nabla\mathbf{v}_T} + \widetilde{\mathbf{v}_C\cdot\nabla\mathbf{v}_C} + \widetilde{(\nabla\cdot\mathbf{v}_C)\mathbf{v}_C}\right], \tag{12b}$$

$$M_3 = -\mathrm{Ro}\left[\widetilde{v_{T_i}}\left(\widetilde{v_{T_i}\mathbf{v}_T} + \widetilde{v_{C_i}\mathbf{v}_C}\right) + \widetilde{v_{C_i}}\left(\widetilde{v_{T_i}\mathbf{v}_C} + \widetilde{v_{C_i}\mathbf{v}_T}\right) + \mathrm{Bu}\widetilde{p_C}\left(\mathbf{v}_T\widetilde{p_C}\right)\right], \tag{12c}$$

$$\widetilde{\Pi_T} = -\mathrm{Ro}\frac{1}{2}\left(\widetilde{\frac{\partial v_{T_i}}{\partial x_k}} + \widetilde{\frac{\partial v_{T_k}}{\partial x_i}}\right)\widetilde{v_{T_i}v_{T_k}}, \tag{12d}$$

$$\widetilde{\Pi_C} = -\mathrm{Ro}\frac{1}{2}\left(\widetilde{\frac{\partial v_{T_i}}{\partial x_k}} + \widetilde{\frac{\partial v_{T_k}}{\partial x_i}}\right)\widetilde{v_{C_i}v_{C_k}} + \mathrm{Ro}\frac{1}{2}\left(\widetilde{\frac{\partial v_{C_i}}{\partial x_k}} + \widetilde{\frac{\partial v_{C_k}}{\partial x_i}}\right)\left(\widetilde{v_{T_i}v_{C_k}} + \widetilde{v_{C_i}v_{T_k}}\right) + \mathrm{Ro}\widetilde{v_{C_i}}\left(\widetilde{v_{T_i}\frac{\partial v_{C_k}}{\partial x_k}}\right) + \mathrm{RoBu}\left(\widetilde{v_{T_k}p_C}\right)\widetilde{\frac{\partial p_C}{\partial x_k}}. \tag{12e}$$

Above, we used index notation for convenience, where v_i represents the ith component of the vector $\mathbf{v}$, and repeated indices imply summation over that index. On the left-hand side of (11), the first term gives the rate of change of large-scale filtered energy $\tilde{e}$, while the second term is the advection of $\tilde{e}$ over the domain by the barotropic flow. The first three terms on the right-hand side of (11) vanish when integrated over the domain, and thus these terms do not contribute to the transfer of energy across scales. Downscale transfer of energy is caused by the next two terms, $\widetilde{\Pi_C}$ and $\widetilde{\Pi_T}$. The barotropic flux, $\widetilde{\Pi_T}$, has contribution from the barotropic mode alone, while baroclinic flux, $\widetilde{\Pi_C}$, has contributions from both barotropic and baroclinic modes.

We note that the above equations are similar to those discussed in Thomas and Vishnu (2022), specifically (8) and (9) there, describing energy transfer across scales. However, there are minor differences. The energy evolution equation given in (11) has an extra advection term on the left-hand side, and this leads to M_1 having an additional term above, compared to that in Thomas and Vishnu (2022). Nevertheless, when integrated over the domain, the equations given here and the ones given in Thomas and Vishnu (2022) are identical as the advection term integrates to zero.

To get a better understanding of the stages of vortex disintegration corresponding to the case highlighted in Fig. 9 for the anticyclone, the physical structure of vorticity ζ_T, flux $\widetilde{\Pi_C}(k_L = 40)$, and pointwise dissipation d_T at four different times are shown in Fig. 11, these corresponding to the four different times highlighted by the red dots in the dissipation curve in Fig. 9b. The pointwise dissipation is computed as $d_T = -\nu\psi_T\Delta^8\zeta_T$. Note that we use the lower case variable d_T to denote pointwise dissipation, while the corresponding domain-integrated value is represented using the upper case variable D_T in (9). Here onward, we will denote $\widetilde{\Pi_C}(k_L = 40)$ by $\widetilde{\Pi_{C_{40}}}$, simplifying the notation. Below, we will specifically look at the anticyclone, since the cyclonic case had qualitatively similar features.

Notice that at $t = 6$, Fig. 11a shows the formation of vorticity filaments discussed earlier, this visualization being the same as that given in Fig. 5d. Notably, we see localized patterns in the flux $\widetilde{\Pi_{C_{40}}}$ in Fig. 11e and barotropic dissipation d_T in Fig. 11i in the same regions where the filaments in the vortex initiate. The filament-forming region is therefore the location where energy transfer from the large initialized vortex scale to dissipative scales begins. Pointwise dissipation can take positive and negative values, although domain-integrated dissipation is positive definite. Nevertheless, we found that only a small fraction of the domain had negative values for d_T, these negative values being much smaller in magnitude than the more frequently occurring high positive d_T values in the domain. The log scale we use for dissipation therefore discards the few negative values of d_T.

Going to Figs. 11b and 11c, corresponding to $t = 10$ and $t = 16$, we see a wider spread in the small-scale vorticity structures associated with the vortex disintegration. Alongside these, we find that $\widetilde{\Pi_{C_{40}}}$ and d_T have corresponding high values in the same spatial locations at these times. Closely examining Fig. 11k, we see that dissipation is higher at the outermost boundaries of the structures formed as a result of the vortex disintegration. We found this to be a consistent feature on examining multiple frames: As the vortex disintegrates, the small-scale structures

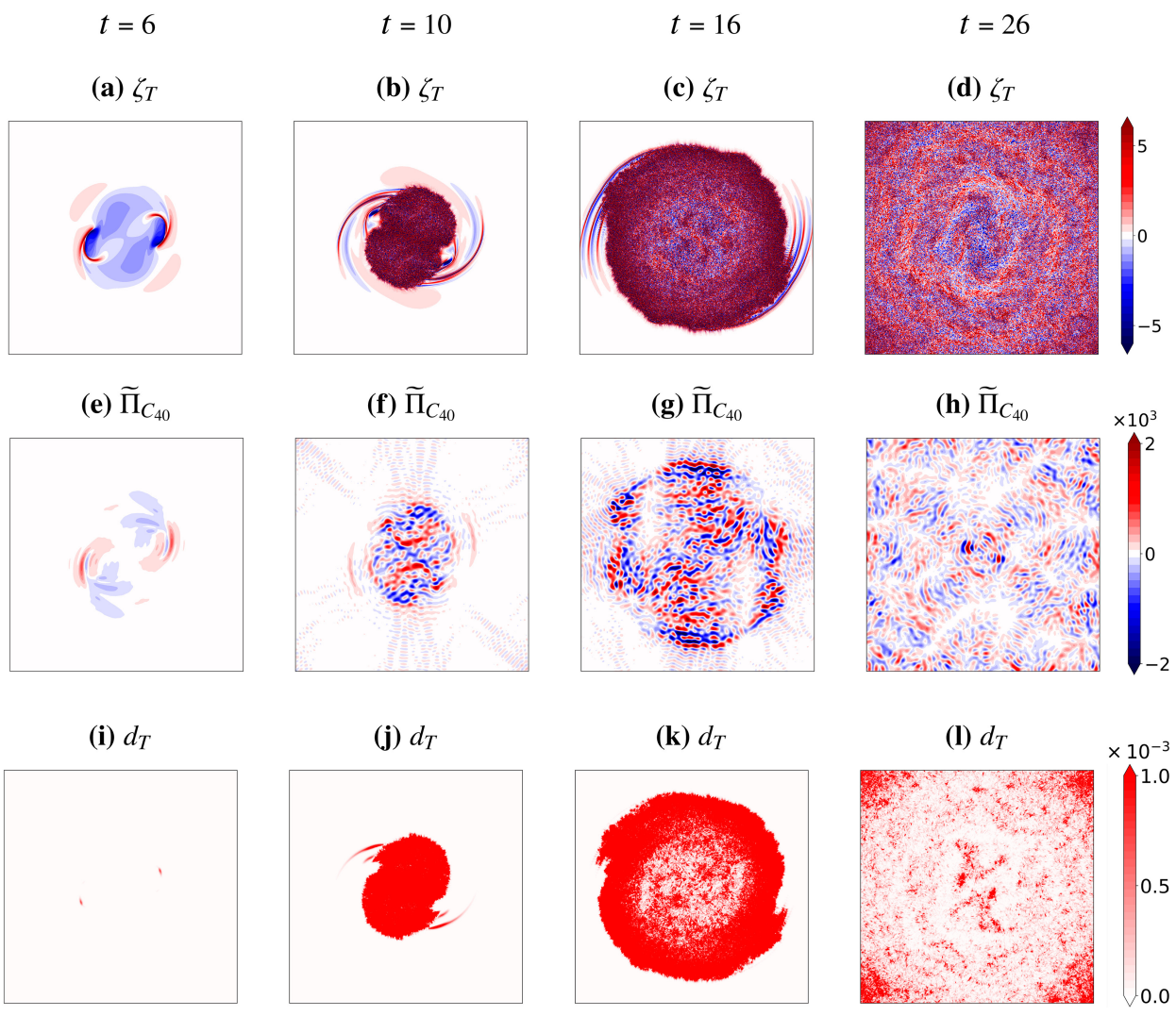

FIG. 11. The three rows show ζ_T, $\widetilde{\Pi_{C_{40}}}$, and d_T for anticyclone with Ro = 0.5 and for initial $E_C/E_T = 6$ at times marked by the red dots in Fig. 9b.

propagate outwards, and high dissipation values were associated with the boundaries of the region that contain small-scale structures. This shows that the formation of small-scale structures from the coherent vortex is accompanied by an increased rate of dissipation. By the time $t = 26$, Fig. 11d shows that the domain is filled with small-scale structures. The corresponding $\widetilde{\Pi_{C_{40}}}$ and d_T fields shown in Figs. 11h and 11l are significantly weaker compared to the previous panels and are spread all over the domain. Comparing the findings from Fig. 11 to Fig. 9b, we see that the time interval during which most of the dissipation occurs—i.e., the interval between the first and last red dots in Fig. 9b—coincides with the interval during which small-scale structures first appear and grow outwards, filling up the whole domain. The small-scale structures are much closer to the dissipation scales and, as a result, are more affected by dissipation.

As mentioned earlier, we described the details of the disintegration process for the anticyclone, although the cyclone had qualitatively similar features. An important difference, as inferred from Fig. 9b, is that although the disintegration process starts early for the anticyclone than the cyclone, the total time taken for the whole process of disintegration from start to end is larger for the anticyclones when compared to cyclones.

Following the above discussion, Fig. 12a shows the domain-integrated $\widetilde{\Pi_{C_{40}}}$, domain-integrated total dissipation $D = D_T + D_C$, and $\mathrm{Ro}_{\mathrm{eff}}$, for the anticyclone with Ro = 0.5 and initial $E_C/E_T = 6$. The effective Rossby number is defined as $\mathrm{Ro}_{\mathrm{eff}} = \mathrm{Ro}\zeta_{\mathrm{RMS}}$, where ζ_{RMS} is the root-mean-square of ζ_T. This is a dynamically evolving Rossby number and is the nondimensional form of the root-mean-square of barotropic vorticity normalized by the inertial frequency. We scaled $\mathrm{Ro}_{\mathrm{eff}}$ by dividing it by 10 to fit it in the same plot and compare it with D and $\tilde{\Pi}_{C_{40}}$. Notice that the blue, red, and black curves, corresponding to $\mathrm{Ro}_{\mathrm{eff}}$, $\widetilde{\Pi_{C_{40}}}$, and D, all are more or less synchronized, with all these variables attaining high values around the same time. This is

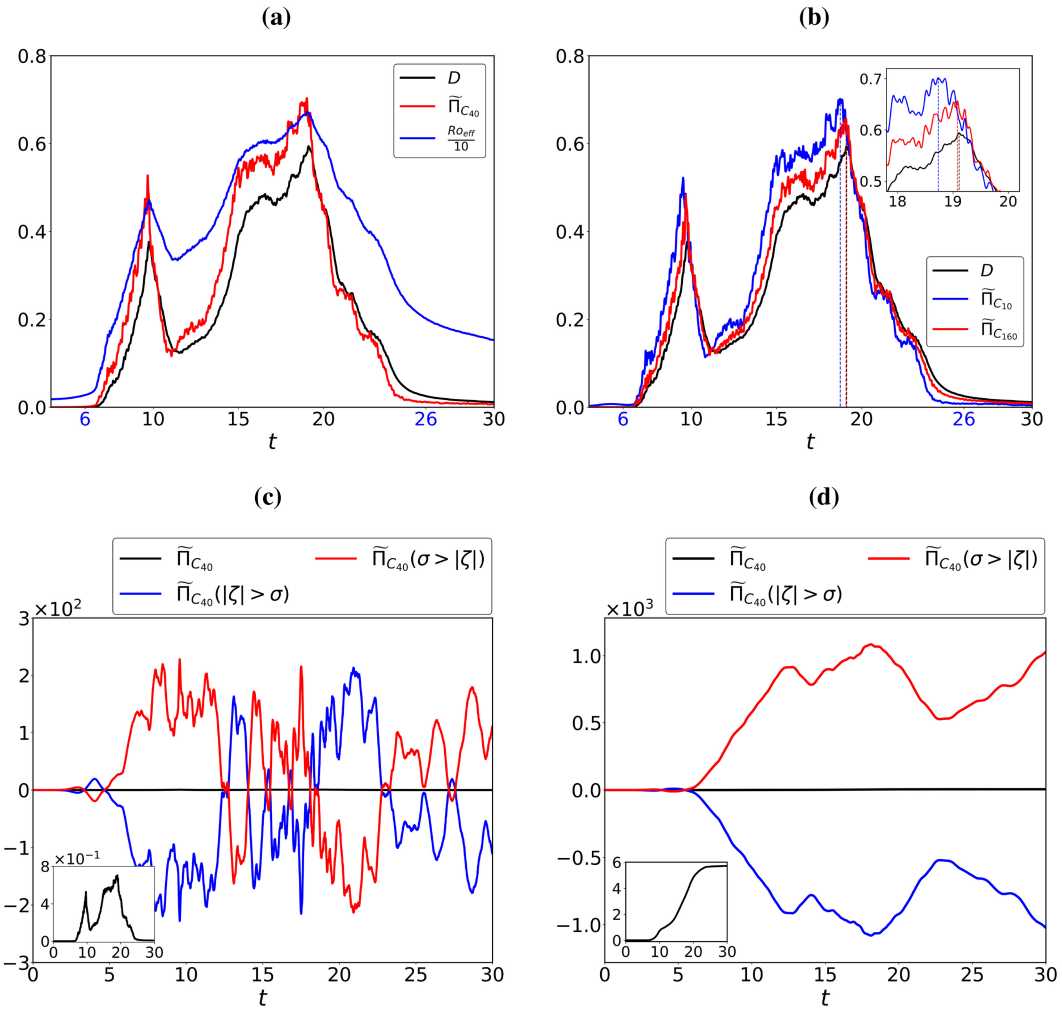

FIG. 12. Figure is for the regime Ro = 0.5 with initial $E_C/E_T = 6$. (a) Domain-integrated total dissipation D, flux $\widetilde{\Pi_{C_{40}}}$, and effective Rossby number $\mathrm{Ro_{eff}}$, and (b) D, $\widetilde{\Pi_{C_{10}}}$, and $\widetilde{\Pi_{C_{160}}}$. (c) Flux $\widetilde{\Pi_{C_{40}}}$ for $|\zeta| > \sigma$ and $\sigma > |\zeta|$ regions, represented by the blue and red curves, respectively. The inset shows the sum of flux in $|\zeta| > \sigma$ and $\sigma > |\zeta|$ regions; this matches the red curve in (a). (d) Time-integrated fluxes in the different regions from (c) and their sum, this being highlighted in the inset.

similar to what was seen in physical space in Fig. 11, where ζ_T, $\widetilde{\Pi_{C_{40}}}$, and d_T attained spatially high values at the same time as the vortex disintegrated. The red curve in Fig. 12a being positive reconfirms a forward energy cascade, with energy being transferred from large scales to small scales as the vortex disintegrates. The energy in the small scales then gets dissipated, and, as a result, we see high values for the black curve showing total dissipation, D.

It can be observed in Fig. 12a that the shapes of the red and black curves closely resemble each other, with the peaks in the red curve appearing slightly earlier in time than those of the black curve. This implies a time delay between dissipation and energy flux, highlighting that the cascade is scale-local, and therefore some nonzero time interval is needed for energy to cascade across scales and reach dissipative scales. Such a time delay has been identified in different turbulent flows in the past, including three-dimensional homogeneous isotropic turbulence and two-dimensional dispersive wave turbulence in rotating shallow water (see specific discussions in Cardesa et al. 2015; Khurshid et al. 2021; Thomas et al. 2024). To highlight this feature more clearly, Fig. 12b shows $\widetilde{\Pi_{C_{10}}}$, $\widetilde{\Pi_{C_{160}}}$, and D. The shapes of blue, red, and black curves, corresponding to $\widetilde{\Pi_{C_{10}}}$, $\widetilde{\Pi_{C_{160}}}$, and D, resemble each other. We further identified the time at which each of the three curves peak, and these are marked as dashed vertical lines and are further zoomed in, in the inset of Fig. 12b. It can be noticed that the blue dashed vertical line corresponding to $\widetilde{\Pi_{C_{10}}}$ appears before the red dashed vertical line, which corresponds to $\widetilde{\Pi_{C_{160}}}$. The black dashed vertical line corresponding to the peak of D appears later. The energy flux associated with scales $k \leq 10$ therefore peaks first, followed by the energy flux associated with scales $k \leq 160$, and then dissipation. This time delay highlights the local nature of the energy cascade and that the energy takes some time to go from the

large-scale structures to small dissipative scales as the vortex disintegrates.

As before, we split the flux into contributions from strain-dominant and vorticity-dominant regions, and these are shown in Fig. 12c. Similar to the energy transfer term seen in the bottom row of Fig. 10, we see that the fluxes in the two different regions are highly oscillatory in nature. We therefore integrated the flux over time, and these are shown in Fig. 12d. Notice that the flux is positive in strain-dominant regions and negative in vorticity-dominant regions. Interaction with the baroclinic flow therefore leads to a downscale energy transfer in strain-dominant regions, while an upscale transfer takes place in vorticity-dominant regions. Since the downscale transfer magnitude is slightly higher than the upscale transfer magnitude, we see a net forward energy cascade. It is striking to note that the fluxes in the two regions are almost three orders of magnitude higher than the total flux, this feature being seen in the bottom row of Fig. 12.

The significance of strain-dominant regions noted above with regards to the forward energy cascade of the flow is something that has been recognized in multiple past studies. Using the same two-vertical-mode model as the one we are using, but in a forced-dissipative setting, Thomas and Vishnu (2022) found that downscale energy transfers were associated with strain-dominant regions. A similar result has been found in observational studies of Yang et al. (2017) and Savage et al. (2025), where forward cascades of the flow localized around strain-dominant regions have been identified. Note that all these are studies that have examined features of eddies and waves in configurations different from the one we are exploring, where vortices disintegrate and dissipate. Nevertheless, we see similarity in the feature that the forward energy flux is concentrated in strain-dominant regions. The commonality of this result implies that observational studies looking for dissipation hotspots in oceanic flows with wave–eddy interactions should pay more attention to strain-dominant regions of the flow.

b. *Energy transfer and dissipation with varying Rossby number and energy ratio*

Having looked at energy transfers and dissipation for a particular case, we will now examine the changes seen as we vary the Rossby number and energy ratio. Top row of Fig. 13 shows the variation in barotropic dissipation D_T with Ro and energy ratio. In Fig. 13a, we see the case of $(E_C/E_T)_{t=0} = 6$ for Ro = 0.2, 0.5, and 0.8. We see that increasing Rossby number narrows the prominent dissipation time window and also increases the maximum dissipation. A similar trend is seen in Fig. 13b for increasing energy ratio with fixed Ro = 0.5. These trends are qualitatively similar for anticyclone and cyclones, although, as noted earlier, cyclones' dissipation peak later in time than anticyclones.

Domain- and time-integrated (from $t = 0$ to 300) values of energy transfer T_{TC} and dissipation D_T for three different Ro values across different $(E_C/E_T)_{t=0}$ are given in Figs. 13c and 13d. We see that the energy transfer and dissipation are extremely low in the lowest energy ratio regimes, these being regimes where the vortex does not disintegrate. With increasing energy ratio, we see that both energy transfer and dissipation increase monotonically, this being the case for anticyclones and cyclones. For all these cases, we found that energy transfers were from baroclinic-to-barotropic mode in vorticity-dominated regions and the opposite way in strain-dominated regions. Additionally, dissipation was found to be higher in strain-dominated regions, as in the previous cases we explored in detail.

Fractional changes in baroclinic and barotropic energy over $t = 0$–300 for three different Ro values across different $(E_C/E_T)_{t=0}$ are given in Figs. 13e and 13f. Looking at Fig. 13e, we see that the baroclinic mode loses energy, the energy loss increasing monotonically with Rossby number and energy ratio. An exception to this is close to the lowest energy ratio cases, these being cases where no disintegration of the vortex takes place. From Fig. 13f, we see that the fractional change in barotropic energy does not show a clear monotonic increase throughout. Although the energy loss increases with increase in energy ratio initially, it saturates and then starts to fall. This is because the baroclinic-to-barotropic energy transfer exceeds barotropic dissipation, leading to less net loss in barotropic energy at higher energy ratios.

8. Summary and discussion

The world's oceans are filled with coherent balanced eddies that carry a dominant share of the flow kinetic energy. In addition to the balanced eddies, the oceans also host a diverse range of dispersive waves generated as a result of wind and tidal forcing. Inertial oscillations form the lowest frequency component in the unbalanced wave field, primarily excited in the upper ocean by atmospheric winds. They are also seen to be excited in the deeper oceans when eddies interact with lateral or bottom boundaries (Webster 1968; Weller 1982; Alford et al. 2013; Clément et al. 2016). As detailed in the introduction, in an attempt to figure out loss of balance mechanisms associated with geostrophic flows, a broad set of studies have explored inertial oscillations' and near-inertial waves' interactions with balanced flows. The present study was aimed at exploring a specific aspect of the interaction problem: how does the unbalanced flow energy level required to distort, disintegrate, and dissipate a coherent eddy change with increasing Rossby number?

We explored the above question in this work using a two-vertical-mode model where we idealized an eddy as a Gaussian barotropic vortex and considered inertial oscillations confined to a single high baroclinic mode. We then examined inertial oscillation-balanced eddy interactions across 640 regimes obtained by varying the initial baroclinic–barotropic energy ratio, $(E_C/E_T)_{t=0}$, and the flow Rossby number, Ro. Out of the 640 regimes, we initialized an anticyclone in 320 regimes and a cyclone in 320 regimes. We examined the energy ratio required to disintegrate an eddy over regimes with Ro varying from 0.1 to 1 using a criterion based on enstrophy fraction at small scales. Specifically, a vortex was considered to have been disintegrated if 95% or more of its energy was transferred to scales one decade below the domain scale, these small scales containing negligible enstrophy initially.

We found that increasing Rossby number led to vortex disintegration taking place at lower energy ratios. Anticyclones

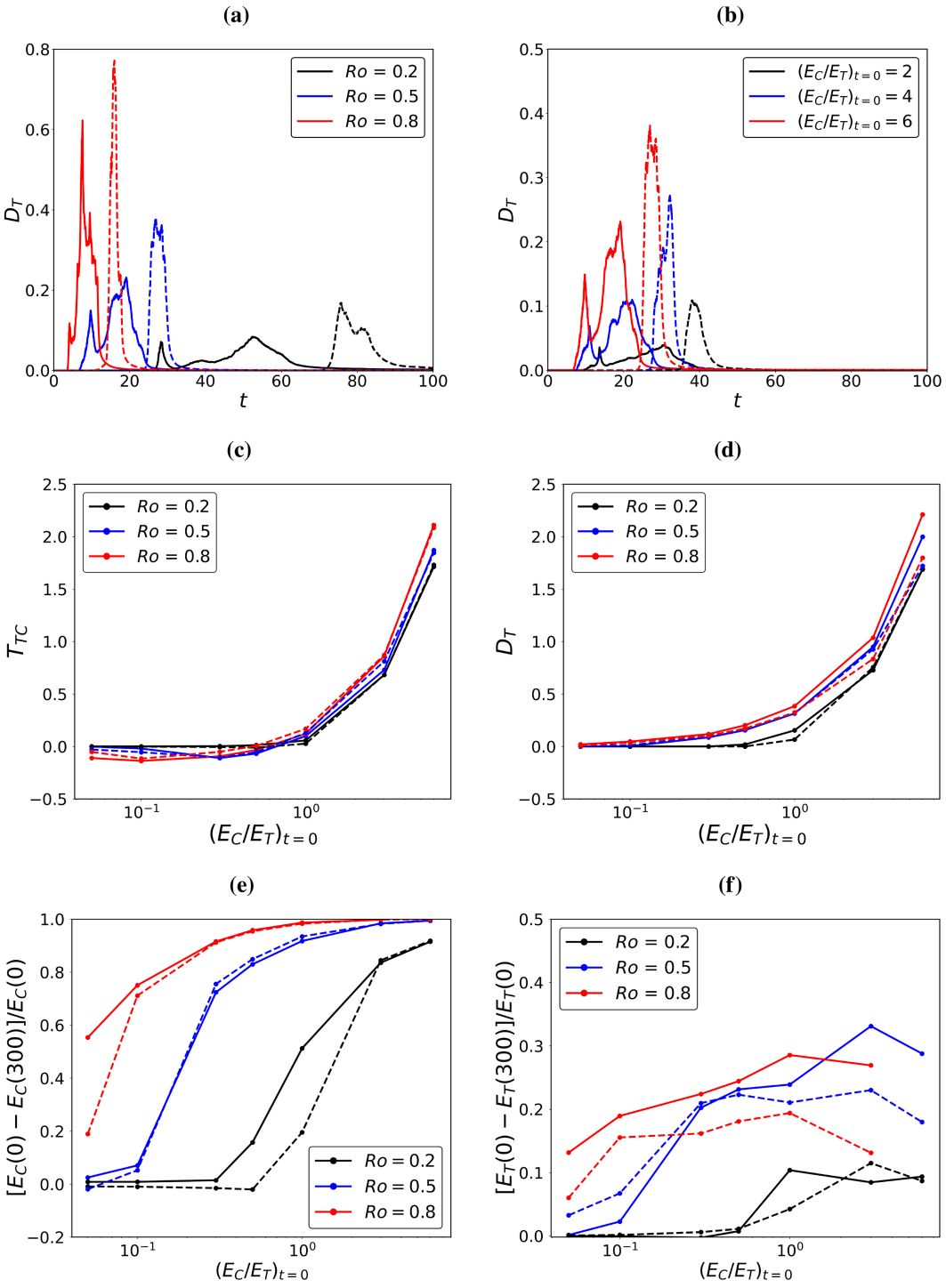

FIG. 13. The barotropic dissipation D_T for (a) different Ro values and initial $E_C/E_T = 6$ and (b) for different initial E_C/E_T ratios and Ro = 0.5. Time-integrated (c) T_{TC} and (d) D_T as a function of initial E_C/E_T for three different Ro values, Ro = 0.2, 0.5, and 0.8. Solid lines are for anticyclones, while dashed lines are for cyclones. The fractional change in (e) E_C and (f) E_T over $t = 0$–300.

were also seen to disintegrate at lower energy ratios than cyclones for a given Rossby number. Looking at the interactions, the disruption of anticyclones started close to the vortex core and then propagated outwards, while the disruption of cyclones started outwards and propagated inwards. We also observed an oscillatory behavior in the inertial oscillation mode's energy with time, which was exclusive to anticyclones. These oscillations decayed and gradually vanished as we

approached energy levels where the vortex disintegrated. Although cyclone cases did not show any such oscillations, the energy in the inertial oscillation mode of cyclone cases also gradually decreased as we got closer to the energy levels where the vortex disintegrated. For cases where the vortex disintegrated, we found that the baroclinic mode transferred energy to the barotropic mode, this energy gain of the barotropic mode proceeded alongside the vortex disintegration process.

Examining the physical field decomposed as strain-dominant and vorticity-dominant regions, we found that baroclinic-to-barotropic energy transfer was associated with vorticity-dominant regions, while strain-dominant regions of the barotropic flow lost energy to the baroclinic flow. Interestingly, multiple previous studies in other configurations have found the latter transfer, i.e., inertial oscillations extracting energy from balanced eddies in strain-dominant regions. In our setup, we found that this transfer was dominated by barotropic flow gaining energy from the baroclinic mode in vortex-dominant regions. As a result, the barotropic flow gained energy as it evolved toward disintegration.

We computed the energy flux in physical space and partitioned it into strain-dominant and vorticity-dominant regions. This decomposition showed that the strain-dominant regions were associated with a downscale energy flux, while vorticity-dominant regions were associated with an upscale energy flux. These are also features identified in a variety of previous studies in different configurations. In our setting, we found that the forward flux in strain-dominant regions slightly dominated over the inverse flux in vorticity-dominant regions, leading to a net forward cascade of the flow energy. We also observed a time delay between dissipation and energy flux from large scales to small scales. Energy which was initially present in large scales is cascaded into smaller scales until it reaches scales where dissipation becomes significant. This results in the energy flux being slightly ahead in time compared to dissipation.

As discussed in section 2, we anticipate multiple differences between this study using a reduced two-vertical-mode model and an equivalent fully three-dimensional study. Two differences are worth emphasizing here. First, inertia–gravity waves in three-dimensions can cascade more efficiently than in two dimensions, due to the nature of their dispersion relationships (see discussions on this aspect in Thomas et al. 2024). To appreciate the second point, consider a three-dimensional inertial oscillation field that is confined to the upper ocean. Projecting it onto a single high baroclinic mode will lead to inertial oscillations with much lower strength in two dimensions, these being excited by the initialization procedure described in section 3. As a result, the three-dimensional energy of an inertial oscillation field corresponding to the two-dimensional inertial oscillation considered in this work is expected to be much larger. Due to these two effects, namely, the more efficient cascade of wave energy in three dimensions and the higher energy of waves in three dimensions corresponding to the two-dimensional cases explored here, for a given Rossby number, we anticipate much higher wave–balance energy ratios to disintegrate coherent vortices than the estimates seen in this study, i.e., from Fig. 3.

Despite the above mentioned points, we anticipate several qualitative features seen in this study to be valuable for future work. Specifically, vortices disintegrating at lower energy ratios at higher Rossby numbers, the differences in energy levels needed to disintegrate anticyclones and cyclones, and the roles played by strain-dominant and vorticity-dominant regions with regards to energy transfers between modes and across scales are noteworthy features that came out of this study. Additionally, the significance of strain-dominant regions for energy extraction by baroclinic flow containing inertial oscillations and the downscale cascade of flow energy are features seen in other past studies operating in different configurations. These insights on the role of different flow regions based on flow partitioning can assist in efficiently locating regions of downscale energy flux, high dissipation, and small-scale mixing during observational cruises.

Acknowledgments. JT gratefully acknowledges financial support from the Deep Ocean Mission scheme of the Ministry of Earth Sciences through the project F. No. MoES/PAMC/DOM/18/2022 (E-12926) and the Naval Research Board through the project NRB-558/OEP/25-26.

Data availability statement. The datasets used to generate results in this manuscript can be accessed at https://doi.org/10.5281/zenodo.20422046.

APPENDIX

Alternate Criteria to Characterize Vortex Disintegration

We used the enstrophy fraction to quantify vortex disintegration earlier. As described there, vortex disintegration takes place with significant changes in the vortex, and these changes can be characterized by other metrics as well. Here, we will use another metric based on azimuthal variability of the vorticity field to quantify vortex disintegration.

Consider the Fourier expansion of the vorticity in azimuthal angles:

$$\zeta(r,\,\theta,\,t) = \sum_{m=0}^{\infty} \hat{\zeta}_m(r,\,t)e^{im\theta}. \tag{A1}$$

Initially, since the vortex is a Gaussian, only $m = 0$ mode contributes to above sum. In other words, $\hat{\zeta}_m(r, 0) = 0$ for all $m > 0$. However, as the vortex gets distorted due to interactions, higher modes get excited. For each mode m, we construct an averaged amplitude as

$$C_m(t) = \sqrt{\frac{\int_0^R |\hat{\zeta}_m(r,\,t)|^2 r dr}{\int_0^R r\,dr}}, \tag{A2}$$

where R is the maximum radial extent of the domain. We then define the fraction of amplitude associated with modes greater than 0 as

$$\xi(t) = \frac{\sum_{m>0} C_m}{\sum_m C_m}. \tag{A3}$$

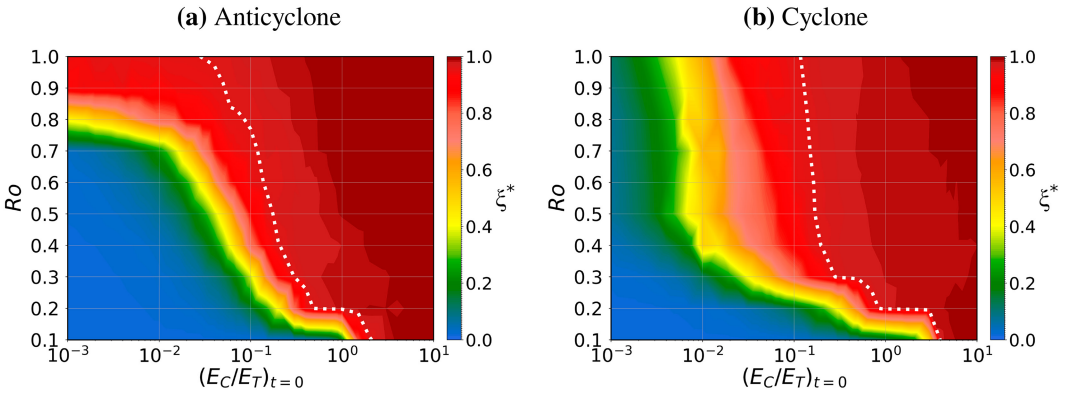

FIG. A1. Figure shows the regime of (a) anticyclonic and (b) cyclonic vortices based on azimuthal distribution of vorticity. The broken white lines indicate contours of 96% ξ^*.

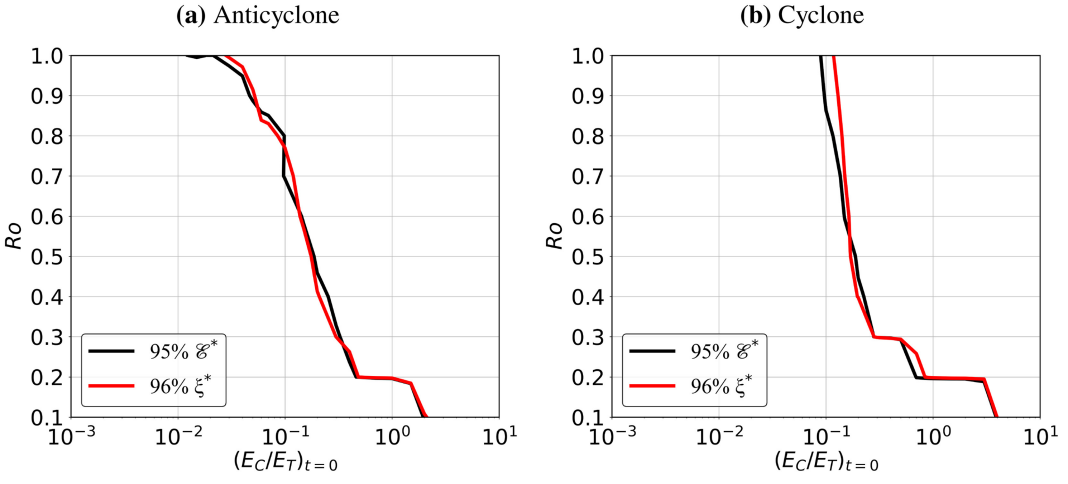

FIG. A2. Figure shows the comparison of vortex disintegration captured using azimuthal distribution of vorticity and enstrophy criteria for (a) anticyclonic and (b) cyclonic cases.

Since the initial vortex has no variability across azimuthal angles, we have $\xi(0) = 0$. However, distortion of the vortex due to interactions leads to ξ increasing with time. We define ξ^* as the maximum value of ξ attained during the time window t = 0–300. Figure A1 shows contours of ξ^* for different Rossby number–energy ratio regimes, these contour plots for anticyclone and cyclone being made in a similar fashion to those shown in Fig. 2 that uses the enstrophy fraction. The broken white lines show 96% lines of ξ^*. Figure A2 shows 96% lines of ξ^* and 95% lines of the enstrophy ratio, the latter being the same lines from Fig. 3a. Notice that the two match reasonably well. This comparison highlights that one could also use ξ^* with a suitable threshold to define and quantify vortex disintegration, the same way we used the enstrophy fraction earlier.

REFERENCES

Alford, M. H., 2001: Internal swell generation: The spatial distribution of energy flux from the wind to mixed layer near-inertial motions. *J. Phys. Oceanogr.*, **31**, 2359–2368, https://doi.org/10.1175/1520-0485(2001)031<2359:ISGTSD>2.0.CO;2.

——, A. Y. Shcherbina, and M. C. Gregg, 2013: Observations of near-inertial internal gravity waves radiating from a frontal jet. *J. Phys. Oceanogr.*, **43**, 1225–1239, https://doi.org/10.1175/JPO-D-12-0146.1.

Arbic, B. K., and Coauthors, 2009: Estimates of bottom flows and bottom boundary layer dissipation of the oceanic general circulation from global high-resolution models. *J. Geophys. Res.*, **114**, C02024, https://doi.org/10.1029/2008JC005072.

Barkan, R., K. B. Winters, and J. C. McWilliams, 2017: Stimulated imbalance and the enhancement of eddy kinetic energy dissipation by internal waves. *J. Phys. Oceanogr.*, **47**, 181–198, https://doi.org/10.1175/JPO-D-16-0117.1.

Brunner-Suzuki, A.-M. E. G., M. A. Sundermeyer, and M.-P. Lelong, 2012: Vortex stability in a large-scale internal wave shear. *J. Phys. Oceanogr.*, **42**, 1668–1683, https://doi.org/10.1175/JPO-D-11-0137.1.

Cao, H., Z. Jing, B. Fox-Kemper, T. Yan, and Y. Qi, 2019: Scale transition from geostrophic motions to internal waves in the northern South China Sea. *J. Geophyts. Res. Oceans*, **124**, 9364–9383, https://doi.org/10.1029/2019JC015575.

Capet, X., J. C. McWilliams, M. J. Molemaker, and A. F. Shchepetkin, 2008: Mesoscale to submesoscale transition in the California Current System. Part III: Energy balance and flux. *J. Phys. Oceanogr.*, **38**, 2256–2269, https://doi.org/10.1175/2008JPO3810.1.

Cardesa, J. I., A. Vela-Martin, S. Dong, and J. Jimenez, 2015: The temporal evolution of the energy flux across scales in homogeneous turbulence. *Phys. Fluids*, **27**, 111702, https://doi.org/10.1063/1.4935812.

Chelton, D. B., M. G. Schlax, R. M. Samelson, and R. A. de Szoeke, 2007: Global observations of large oceanic eddies. *Geophys. Res. Lett.*, **34**, L15606, https://doi.org/10.1029/2007GL030812.

Clément, L., E. Frajka-Williams, K. L. Sheen, J. A. Brearley, and A. C. Naveira Garabato, 2016: Generation of internal waves by eddies impinging on the western boundary of the North Atlantic. *J. Phys. Oceanogr.*, **46**, 1067–1079, https://doi.org/10.1175/JPO-D-14-0241.1.

Danioux, E., J. Vanneste, and O. Bühler, 2015: On the concentration of near-inertial waves in anticyclones. *J. Fluid Mech.*, **773**, R2, https://doi.org/10.1017/jfm.2015.252.

Elipot, S., R. Lumpkin, and G. Prieto, 2010: Modification of inertial oscillations by the mesoscale eddy field. *J. Geophys. Res.*, **115**, C09010, https://doi.org/10.1029/2009JC005679.

Flierl, G. R., 1988: On the instability of geostrophic vortices. *J. Fluid Mech.*, **197**, 349–388, https://doi.org/10.1017/S0022112088003283.

Frierson, D. M. W., A. J. Majda, and O. M. Pauluis, 2004: Large scale dynamics of precipitation fronts in the tropical atmosphere: A novel relaxation limit. *Commun. Math. Sci.*, **2**, 591–626, https://doi.org/10.4310/CMS.2004.v2.n4.a3.

Gertz, A., and D. N. Straub, 2009: Near-inertial oscillations and the damping of midlatitude gyres: A modeling study. *J. Phys. Oceanogr.*, **39**, 2338–2350, https://doi.org/10.1175/2009JPO4058.1.

Gregg, M. C., T. B. Sanford, and D. P. Winkel, 2003: Reduced mixing from the breaking of internal waves in equatorial waters. *Nature*, **422**, 513–515, https://doi.org/10.1038/nature01507.

Jing, Z., L. Wu, and X. Ma, 2017: Energy exchange between the mesoscale oceanic eddies and wind-forced near-inertial oscillations. *J. Phys. Oceanogr.*, **47**, 721–733, https://doi.org/10.1175/JPO-D-16-0214.1.

——, P. Chang, S. F. DiMarco, and L. Wu, 2018: Observed energy exchange between low-frequency flows and internal waves in the Gulf of Mexico. *J. Phys. Oceanogr.*, **48**, 995–1008, https://doi.org/10.1175/JPO-D-17-0263.1.

Khurshid, S., D. A. Donzis, and K. R. Sreenivasan, 2021: Slow spectral transfer and energy cascades in isotropic turbulence. *J. Fluid Mech.*, **908**, A21, https://doi.org/10.1017/jfm.2020.862.

Lee, D.-K., and P. P. Niiler, 1998: The inertial chimney: The near-inertial energy drainage from the ocean surface to the deep layer. *J. Geophys. Res.*, **103**, 7579–7591, https://doi.org/10.1029/97JC03200.

Lien, R.-C., and T. B. Sanford, 2019: Small-scale potential vorticity in the upper-ocean thermocline. *J. Phys. Oceanogr.*, **49**, 1845–1872, https://doi.org/10.1175/JPO-D-18-0052.1.

MacKinnon, J. A., and Coauthors, 2017: Climate process team on internal wave–driven ocean mixing. *Bull. Amer. Meteor. Soc.*, **98**, 2429–2454, https://doi.org/10.1175/BAMS-D-16-0030.1.

Mariotti, A., B. Legras, and D. G. Dritschel, 1994: Vortex stripping and the erosion of coherent structures in two-dimensional flows. *Phys. Fluids*, **6**, 3954–3962, https://doi.org/10.1063/1.868385.

Nikurashin, M., G. K. Vallis, and A. Adcroft, 2013: Routes to energy dissipation for geostrophic flows in the Southern Ocean. *Nat. Geosci.*, **6**, 48–51, https://doi.org/10.1038/ngeo1657.

Okubo, A., 1970: Horizontal dispersion of floatable particles in the vicinity of velocity singularities such as convergences. *Deep-Sea Res. Oceanogr. Abstr.*, **17**, 445–454, https://doi.org/10.1016/0011-7471(70)90059-8.

Pauluis, O., D. M. W. Frierson, and A. J. Majda, 2008: Precipitation fronts and the reflection and transmission of tropical disturbances. *Quart. J. Roy. Meteor. Soc.*, **134**, 913–930, https://doi.org/10.1002/qj.250.

Pinkel, R., 2014: Vortical and internal wave shear and strain. *J. Phys. Oceanogr.*, **44**, 2070–2092, https://doi.org/10.1175/JPO-D-13-090.1.

Provenzale, A., 1999: Transport by coherent barotropic vortices. *Annu. Rev. Fluid Mech.*, **31**, 55–93, https://doi.org/10.1146/annurev.fluid.31.1.55.

Qiu, B., T. Nakano, S. Chen, and P. Klein, 2017: Submesoscale transition from geostrophic flows to internal waves in the northwestern Pacific upper ocean. *Nat. Commun.*, **8**, 14055, https://doi.org/10.1038/ncomms14055.

——, ——, ——, and ——, 2022: Bi-directional energy cascades in the Pacific Ocean from equator to Subarctic Gyre. *Geophys. Res. Lett.*, **49**, e2022GL097713, https://doi.org/10.1029/2022GL097713.

Rocha, C. B., G. L. Wagner, and W. R. Young, 2018: Stimulated generation: Extraction of energy from balanced flow by near-inertial waves. *J. Fluid Mech.*, **847**, 417–451, https://doi.org/10.1017/jfm.2018.308.

Savage, A. C., and Coauthors, 2017: Frequency content of sea surface height variability from internal gravity waves to mesoscale eddies. *J. Geophys. Res. Oceans*, **122**, 2519–2538, https://doi.org/10.1002/2016JC012331.

——, A. F. Waterhouse, J. A. MacKinnon, X. Yu, A. C. Naveira Garabato, D. G. Evans, E. Frajka-Williams, and L. N. Thomas, 2025: Observations of upper-ocean kinetic energy transfers between near-inertial internal waves and low-frequency dynamics. *J. Phys. Oceanogr.*, **55**, 1625–1643, https://doi.org/10.1175/JPO-D-23-0230.1.

Shcherbina, A. Y., E. A. D'Asaro, C. M. Lee, J. M. Klymak, M. J. Molemaker, and J. C. McWilliams, 2013: Statistics of vertical vorticity, divergence, and strain in a developed submesoscale turbulence field. *Geophys. Res. Lett.*, **40**, 4706–4711, https://doi.org/10.1002/grl.50919.

Stechmann, S. N., and A. J. Majda, 2006: The structure of precipitation fronts for finite relaxation time. *Theor. Comput. Fluid Dyn.*, **20**, 377–404, https://doi.org/10.1007/s00162-006-0014-1.

Sutyrin, G. G., 2019: On vortex intensification due to stretching out of weak satellites. *Phys. Fluids*, **31**, 075103, https://doi.org/10.1063/1.5098068.

Taylor, S., and D. Straub, 2020: Effects of adding forced near-inertial motion to a wind-driven channel flow. *J. Phys. Oceanogr.*, **50**, 2983–2996, https://doi.org/10.1175/JPO-D-19-0299.1.

Tchilibou, M., L. Gourdeau, R. Morrow, G. Serazin, B. Djath, and F. Lyard, 2018: Spectral signatures of the tropical Pacific dynamics from model and altimetry: A focus on the meso-/submesoscale range. *Ocean Sci.*, **14**, 1283–1301, https://doi.org/10.5194/os-14-1283-2018.

Thomas, J., 2023: Turbulent wave-balance exchanges in the ocean. *Proc. Roy. Soc.*, **479A**, 20220565, https://doi.org/10.1098/rspa.2022.0565.

——, and R. Yamada, 2019: Geophysical turbulence dominated by inertia–gravity waves. *J. Fluid Mech.*, **875**, 71–100, https://doi.org/10.1017/jfm.2019.465.

——, and S. Arun, 2020: Near-inertial waves and geostrophic turbulence. *Phys. Rev. Fluids*, **5**, 014801, https://doi.org/10.1103/PhysRevFluids.5.014801.

——, and D. Daniel, 2020: Turbulent exchanges between near-inertial waves and balanced flows. *J. Fluid Mech.*, **902**, A7, https://doi.org/10.1017/jfm.2020.510.

——, and R. Vishnu, 2022: Turbulent transition of a flow from small to $O(1)$ Rossby numbers. *J. Phys. Oceanogr.*, **52**, 2609–2625, https://doi.org/10.1175/JPO-D-21-0270.1.

——, K. S. Smith, and O. Bühler, 2017: Near-inertial wave dispersion by geostrophic flows. *J. Fluid Mech.*, **817**, 406–438, https://doi.org/10.1017/jfm.2017.124.

——, R. S. Rajpoot, and P. Gupta, 2024: The turbulent cascade of inertia-gravity waves in rotating shallow water. *J. Fluid Mech.*, **1000**, A30, https://doi.org/10.1017/jfm.2024.854.

Torres, H. S., P. Klein, D. Menemenlis, B. Qiu, Z. Su, J. Wang, S. Chen, and L.-L. Fu, 2018: Partitioning ocean motions into balanced motions and internal gravity waves: A modeling study in anticipation of future space missions. *J. Geophys. Res. Oceans*, **123**, 8084–8105, https://doi.org/10.1029/2018JC014438.

Viúdez, A., 2021: Robust and unstable axisymmetric vortices, including neutral vortices, of a new two-dimensional vortex family. *Phys. Fluids*, **33**, 054103, https://doi.org/10.1063/5.0048128.

Vladoiu, A., R.-C. Lien, and E. Kunze, 2024: Energy partition between submesoscale internal waves and quasigeostrophic vortical motion in the pycnocline. *J. Phys. Oceanogr*, **54**, 1285–1307, https://doi.org/10.1175/JPO-D-23-0090.1.

Wagner, G. L., and W. R. Young, 2016: A three-component model for the coupled evolution of near-inertial waves, quasi-geostrophic flow and the near-inertial second harmonic. *J. Fluid Mech.*, **802**, 806–837, https://doi.org/10.1017/jfm.2016.487.

Watanabe, M., and T. Hibiya, 2002: Global estimates of the wind-induced energy flux to inertial motions in the surface mixed layer. *Geophys. Res. Lett.*, **29**, 1239, https://doi.org/10.1029/2001GL014422.

Webster, F., 1968: Observations of inertial-period motions in the deep sea. *Rev. Geophys.*, **6**, 473–490, https://doi.org/10.1029/RG006i004p00473.

Weiss, J., 1991: The dynamics of enstrophy transfer in two-dimensional hydrodynamics. *Physica D*, **48**, 273–294, https://doi.org/10.1016/0167-2789(91)90088-Q.

Weller, R. A., 1982: The relation of near-inertial motions observed in the mixed layer during the JASIN (1978) experiment to the local wind stress and to the quasi-geostrophic flow field. *J. Phys. Oceanogr.*, **12**, 1122–1136, https://doi.org/10.1175/1520-0485(1982)012<1122:TRONIM>2.0.CO;2.

Whalen, C. B., C. de Lavergne, A. C. Naveira Garabato, J. M. Klymak, J. A. MacKinnon, and K. L. Sheen, 2020: Internal wave-driven mixing: Governing processes and consequences for climate. *Nat. Rev. Earth Environ.*, **1**, 606–621, https://doi.org/10.1038/s43017-020-0097-z.

Yang, Q., W. Zhao, X. Liang, J. Dong, and J. Tian, 2017: Elevated mixing in the periphery of mesoscale eddies in the South China Sea. *J. Phys. Oceanogr.*, **47**, 895–907, https://doi.org/10.1175/JPO-D-16-0256.1.

Yu, X., A. L. Ponte, S. Elipot, D. Menemenlis, E. D. Zaron, and R. Abernathey, 2019: Surface kinetic energy distributions in the global oceans from a high-resolution numerical model and surface drifter observations. *Geophys. Res. Lett.*, **46**, 9757–9766, https://doi.org/10.1029/2019GL083074.

Zhai, X., H. L. Johnson, and D. P. Marshall, 2010: Significant sink of ocean-eddy energy near western boundaries. *Nat. Geosci.*, **3**, 608–612, https://doi.org/10.1038/ngeo943.